Thermally-Driven Disc Winds as a Mechanism for X-ray Irradiation Heating in Black Hole X-ray Binaries: The Case Study of GX339-4

B.E. Tetarenko, G. Dubus, G. Marcel, C. Done, M. Clavel

Monthly Notices of the ROYAL ASTRONOMICAL SOCIETY

MNRAS **495,** 3666–3682 (2020) doi:10.1093/mnras/staa1367
Advance Access publication 2020 May 20

Thermally driven disc winds as a mechanism for X-ray irradiation heating in black hole X-ray binaries: the case study of GX339–4

B. E. Tetarenko,[1]★ G. Dubus [2], G. Marcel,[3] C. Done[4] and M. Clavel[2]

[1]*Department of Astronomy, University of Michigan, 1085 South University Avenue, Ann Arbor, MI 48109-1107, USA*
[2]*IPAG, CNRS, Université Grenoble Alpes, F-38000 Grenoble, France*
[3]*Department of Physics, Villanova University, Villanova, PA 19085, USA*
[4]*Department of Physics, University of Durham, South Road, Durham DH1 3LE, UK*

Accepted 2020 May 4. Received 2020 April 28; in original form 2019 December 19

ABSTRACT

X-ray irradiation heating of accretion discs in black hole X-ray binaries (BHXBs) plays a key role in regulating their outburst cycles. However, despite decades of theoretical and observational efforts, the physical mechanism(s) responsible for irradiating these discs remains largely unknown. We have built an observation-based methodology to estimate the strength of irradiation of BHXB discs by combining multiwavelength X-ray and optical/infrared (OIR) data throughout transient outbursts. We apply this to ∼15 yr of activity in the Galactic BHXB GX339–4. Our findings suggest that the irradiation heating required by the optical data is large in this system. Direct illumination of the outer disc does not produce sufficient irradiation, but this should also produce a thermal-radiative wind which adds to the irradiation heating by scattering flux down on to the disc. However, analytic estimates of X-ray illumination from scattering in the wind are still not sufficient to produce the observed heating, even in combination with direct illumination. Either the analytic thermal-radiative wind models are underestimating the effect of the wind, or there are additional scattering mechanisms at work, such as magnetically driven outflows, acting to increase the OIR flux. While wind-driven irradiation is likely a common feature among long-period BHXBs, fully understanding the driving mechanism(s) behind such a wind will require radiation hydrodynamic simulations.

Key words: accretion, accretion discs – black hole physics – stars: individual: GX339–4 – stars: winds, outflows – X-rays: binaries.

1 INTRODUCTION

Illumination of the outer accretion disc, by X-rays produced in the inner accretion flow, plays a key role in regulating the outburst cycles of X-ray binary systems (van Paradijs & McClintock 1994; van Paradijs 1996). This X-ray irradiation determines the temperature over most of the accretion disc during outburst and thus, is a major contributor to the thermal balance in the accretion flow of these binary systems. It controls the outburst decay towards quiescence (and thus the overall outburst duration) and sets the limit on the amount of mass able to be accreted during outburst (thus impacting the overall outburst recurrence time-scales) (King & Ritter 1998; Dubus, Hameury & Lasota 2001). As a result, the light curves of X-ray binary outbursts display characteristic profile shapes, that encode within them distinct observational signatures of the X-ray irradiation source heating the disc in the system (King & Ritter 1998; Kim, Wheeler & Mineshige 1999; Dubus et al. 2001; Tetarenko et al. 2018a).

Among X-ray binary systems, black hole low-mass X-ray binaries (BH-LMXBs), offer ideal laboratories in which to understand the mechanism behind the irradiation heating of X-ray binary accretion discs. They undergo bright X-ray ($L_{\rm X,peak} \sim 10^{36}$–$10^{39}$ erg s^{-1}; Chen, Shrader & Livio 1997; Tetarenko et al. 2016) and optical (van Paradijs 1996) outbursts, indicative of episodes of rapid mass transfer from a low-mass ($< 1\,{\rm M}_{\odot}$) companion star on to a stellar-mass ($5-30\,{\rm M}_{\odot}$) BH, which recur frequently on observable month to year time-scales (McClintock & Remillard 2006; Tetarenko et al. 2016). Moreover, the majority of the optical/infrared (OIR) light emitted by the accretion discs in BH-LMXBs comes from reprocessed X-rays (van Paradijs & McClintock 1994; van Paradijs 1996), making the OIR regime the only direct probe of the X-ray irradiating flux we have.

The mechanism behind the bright (X-ray and optical) outbursts observed in BH-LMXBs can be understood using the disc-instability model (DIM; Osaki 1974; Meyer & Meyer-Hofmeister 1981; Smak 1983, 1984; Cannizzo, Wheeler & Ghosh 1985; Mineshige & Wheeler 1989; Cannizzo 1993), with the addition of irradiation and evaporation ('truncation') of the inner thin-disc to a radiatively inefficient flow (DIM+irradiation; Dubus et al. 2001).

★ E-mail: btetaren@umich.edu

The DIM+irradiation predicts that the outburst light curve of a BH-LMXB will show an exponential+linear shaped decay profile. With the exponential-shaped decay, attributed to a viscously accreting irradiated disc, transitioning to a linear-shaped decay when the temperature drops low enough in the outer disc, resulting in the formation and propagation of a cooling front inward at a speed controlled purely by the decaying X-ray-irradiating flux.

Despite being the subject of extensive theoretical and observational work for decades, how X-ray binary discs are irradiated is not well understood. Both the mechanism by which the discs are heated, and the fraction of the X-ray flux that is intercepted and reprocessed in the outer disc (hereafter referred to as $\mathcal{C}$), remain open questions in the field. The reason for this stems from the fact that main factors determining the intercepted fraction remain largely unknown. Such factors include: geometry of the disc and irradiating source, X-ray albedo of the disc, and effect the illuminating spectrum has on thermal properties of the disc itself. Moreover, whether such quantities vary as functions of time and/or disc radius, has not yet been studied extensively.

Note that, throughout this work, $\mathcal{C}$ is defined using the formulation in Dubus et al. 1999. Here, the irradiation temperature is defined as a function of $\dot{M}$ (see equation 4). In the literature, irradiation temperature may also be defined in terms of luminosity (e.g. Dubus et al. 2001). To directly compare values of $\mathcal{C}$ derived via the luminosity formulation, to the $\mathcal{C}$ computed in this paper, one must multiply by an additional factor of accretion efficiency.

Recently, Tetarenko et al. (2018a) analysed the X-ray light curves for a large sample of BH-LMXB outbursts. They derived estimates for $\mathcal{C}$ by comparing the observed X-ray light-curve profiles to the predictions of the DIM+irradiation, assuming a source of X-ray irradiation proportional to the central mass-accretion rate ($\dot{M}_{\rm in}$) throughout outburst. These authors are able to show that an initial exponential-shaped decline after the outburst peak is a robust feature of a fully irradiated disc accreting on a viscous time-scale. However, they also find that the predictions of the DIM+irradiation do not adequately describe the later stages of BH-LMXB outburst light curves.

As a result, they derive values of $\mathcal{C}$ from the X-ray light curves significantly in excess of $\sim 5 \times 10^{-3}$. This is the typical value assumed in theoretical work [Vrtilek et al. 1990 (V90); de Jong, van Paradijs & Augusteijn 1996). This value is also consistent with the amount of X-ray heating required to stabilize persistent X-ray binary systems against the thermal-viscous instability (van Paradijs 1996; Coriat, Fender & Dubus 2012; Tetarenko et al. 2016). Tetarenko et al. (2018a) postulate that this suggests that BH-LMXB X-ray light-curve profiles, beyond the initial exponential decay, are shaped by a variety of physical mechanisms, for which irradiation is only one of them. Examples of such mechanisms include: mass-loss through either inner disc evaporation to a radiatively inefficient structure or mass-loss from an accretion disc wind.

X-ray light curves alone may be insufficent to understand how the X-ray irradiating source heats the discs through the course of BH-LMXB outbursts (Tetarenko et al. 2018a). However, the use of simultaneous multiwavelength data sets does provide a promising alternative approach. By modelling the irradiated discs in BH-LMXBs, assuming a constant irradiation geometry, values of $\mathcal{C} \sim 6 \times 10^{-4} - 7 \times 10^{-3}$ have been found to sufficiently explain the observed multiwavelength outburst behaviour in a small sample of systems (e.g. Hynes et al. 2002; Suleimanov, Lipunova & Shakura 2008; Lipunova & Malanchev 2017). However, evidence also exists suggesting the possibility that $\mathcal{C}$ may change between the hard and soft accretion states (e.g. Gierliński, Done & Page 2009; Kimura & Done 2019). Moreover, a handful of BH-LMXBs show complex light-curve morphology. Here, variability on a range of time-scales (e.g. flaring episodes) and extended plateau phases is observed. These temporal features are suggestive of a non-constant irradiation geometry, where a temporal and/or spatially varying X-ray irradiation source heats the disc (e.g. Esin, Lasota & Hynes 2000a; Esin et al. 2000b).

As such, in this paper we focus on building a numerical methodology that can track the time-series evolution of the X-ray irradiation heating the discs in BH-LMXB systems using a combination of observed X-ray, optical, and infrared light curves. This paper is organized as follows: Section 2 describes the multiwavelength observations, and binary system characteristics, of Galactic BH-LMXB GX339–4 that we make use of in this work. Appendix A summarizes our methodology, while a detailed account describing the development of our methodology is provided in Appendix A. Section 4 describes the application of our methodology to the multiwavelength observations of GX339–4. Section 5 explores the physical mechanism(s) responsible for the irradiation heating of the accretion disc in GX339–4, and Section 6 summarizes this work.

2 THE GALACTIC BHXB GX339–4

GX339–4 is a Galactic LMXB that was discovered during an X-ray outburst in 1972 (Markert et al. 1973). No dynamical mass estimate currently exists for this source. However, both the known mass function (Hynes et al. 2003; Heida et al. 2017), as well as X-ray spectral and temporal properties (Zdziarski et al. 1998; Sunyaev & Revnivtsev 2000), are indicative of the BH nature of the compact object in the system. Over the past nearly half a century, this system has undergone more than 20 individual outbursts. As a result, GX339–4 is one of the most frequently recurring, and in turn one of the most extensively studied, transient X-ray binaries in our Galaxy. During its multitude of outbursts, GX339–4 has been observed to display the entire array of X-ray spectral accretion states, as well as a range of morphology in its X-ray and optical light curves, including combination exponential+linear shaped profiles, extended plateau phases, and multiple flaring episodes during the outburst decay. See Table 14 of Tetarenko et al. (2016) for a complete list of references. For these reasons, GX339–4 is an ideal source for study.

2.1 Observational data

GX339–4 has been extensively observed over the past two decades, at X-ray, optical, and infrared wavelengths, with a combination of the *Rossi X-ray Timing Explorer* (*RXTE*), the *Neil Gehrels Swift Observatory*, the *Monitor of All-sky X-ray Image* (*MAXI*) telescope, and the Small & Moderate Aperture Research Telescope System (SMARTS; Subasavage et al. 2010) 1.3 m telescope in Cerro Tololo, Chile. We have collected all X-ray through infrared data available for GX339–4 during the time period of 2002–2015 from the (i) Proportional Counter Array (PCA) aboard *RXTE*, (ii) X-ray Telescope (XRT) aboard *Swift*, (iii) *MAXI* telescope, and (iv) A Novel Dual Imaging CAMera (ANDICAM; DePoy et al. 2003) aboard the SMARTS 1.3 m telescope. This data set covers nine individual outbursts of GX339–4. See Table 1 and Fig. 1 for outburst information.

2.1.1 *X-ray light curves*

We obtained all *RXTE*/PCA and *MAXI*/GSC data from the WATCHDOG project (Tetarenko et al. 2016). This includes all good pointed

Table 1. Outburst Activity in GX339–4 between 2002-2015.

Outburst Year	$t_{\rm begin}$ (MJD)	$t_{\rm end}$ (MJD)	Data Available	Outburst Type
2002–2003	52350	52750	PCA,ANDICAM	C
2004–2005	53054	53515	PCA,ANDICAM	C
2006	53751	53876	PCA,ANDICAM	F
2006–2007	54053	54391	PCA,XRT,ANDICAM	C
2008	54624	54748	PCA,XRT,ANDICAM	F
2009	54875	55024	PCA,XRT,ANDICAM	F
2009–2011	55182	55665	PCA,XRT,ANDICAM	C
2013	56505	56608	XRT,ANDICAM	F
2014–2015	56936	57311	XRT,GSC,ANDICAM	C

The outburst year, and MJD of the beginning ($t_{\rm begin}$), and end ($t_{\rm end}$) of the outbursts are from the WATCHDOG catalogue (Tetarenko et al. 2016). Outburst type refers to the outburst classifications defined in Tetarenko et al. (2016): C – canonical, cycles through hard and soft accretion states during outburst, and F – failed, remains in the hard accretion state for the duration of the outburst.

PCA observations (i.e. no scans or slews) available (over the *RXTE* mission) in the HEASARC archive and publicly available data from the *MAXI* online archive.[1] All *Swift*/XRT data, including both windowed-timing and photon-counting mode observations, were obtained from the *Swift*/XRT online product builder[2] (Evans et al. 2009).

All X-ray light curves were originally extracted in the 2–10 keV band. These light curves were then converted from instrument specific count-rate to band-limited flux by using crabs as a baseline unit and calculating approximate count rate equivalences in the 2–10 keV band (see Tetarenko et al. 2016 for details on this method).

Next, band-limited flux was converted to bolometric flux by splitting each outburst into individual accretion states using the WATCHDOG project's Accretion-State-By-Day tool,[3] and applying the accretion state specific bolometric corrections estimated by Migliari & Fender (2006). Lastly, by applying an accretion efficiency defined as (Coriat et al. 2012)[4]

$$\eta = \begin{cases} 0.1\left(\frac{\dot{M}}{0.01\dot{M}_{\rm edd}}\right) & L_{\rm X} < 0.01L_{\rm edd} \\ 0.1 & L_{\rm X} \geq 0.01L_{\rm edd}, \end{cases}$$

where the Eddington accretion rate is defined as $L_{\rm edd} = 0.1\dot{M}_{\rm edd}c^2$, bolometric flux was converted to an observed $\dot{M}_{\rm in}$ via

$$\dot{M}_{\rm in} = \frac{F_{\rm X,bol}(4\pi D^2)}{\eta c^2}. \quad (1)$$

2.1.2 OIR light curves

We have collected all available optical and IR observations of GX339–4 from SMARTS/ANDICAM in the *V*, *I*, *J*, and *H* bands. Data from 2002 to 2012 were obtained from Buxton et al. (2012). Additional data covering the time period of 2013–2015 were collected separately. For the reduction procedure used for this data, see Buxton et al. (2012).

Following Buxton et al. (2012), all data were corrected for interstellar extinction according to O'Donnell (1994) (for *V* and *I* bands) and Cardelli, Clayton & Mathis (1989) (for *J* and *H* bands). Magnitudes were dereddened using the SPECUTILS package in PYTHON and $E(B-V) = 1.2 \pm 0.1$ (Zdziarski et al. 1998). The uncertainty on the dereddened magnitudes were calculated by adding the photometric and interstellar reddening errors in quadrature. Lastly, dereddened magnitudes were converted to flux density (in Jy) using the appropriate filter zero points obtained from the SVO filter service.[5] Note that, it is possible the reddening correction used here is overestimated. See Fig. 4, and Section 5, for a discussion of the effect this would have on our results. See also Buxton et al. (2012), for a discussion of other reddening estimates present in the literature for GX339–4. Also see Kosenkov et al. (2020) (which we became aware of after this manuscript was submitted). They use a similar SMARTS data set, though focusing on the non-disc components in the OIR regime.

2.1.3 X-ray spectra

We make use of the spectral fitting and analysis done by Clavel et al. (2016), who have fitted a two-component disc blackbody plus power-law model to all available *RXTE*/PCA spectra in the 3–40 keV band,[6] to compute the (i) bolometric luminosity, $L_{\rm bol}(t)$, and (ii) Compton temperature, $T_{\rm IC}(t)$, as a function of time during outbursts of GX339–4 occurring between 2002–2012. These two quantities are essential input parameters needed to model the evolution, and observable properties, of a thermally driven (Compton-heated) wind in this system. See Section 5 for further discussion. We compute $L_{\rm bol}(t)$ from the 3–200 keV flux, estimated by Marcel et al. (2019) from the best fits to all available *RXTE*/PCA spectra.

We follow the procedure outlined in Shidatsu & Done (2019) to compute $T_{\rm IC}(t)$. Considering each time t_i in which spectral information is available, we integrate the observed (best-fitting) spectral energy distribution (SED) as follows:

$$T_{\rm IC}(t_i) = \frac{\int h\nu F_\nu {\rm d}\nu}{4k\int F_\nu {\rm d}\nu}, \quad (2)$$

where k is the Boltzmann constant. Here, we set the lower limit of the integral at 0.1 keV. The dependence of the Compton temperature on the high-energy cutoff (for a power law) saturates at >100 keV as a result of the rollover in the Klein–Nishima cross-section compared to the constant cross-section assumed in Thomson scattering (Done, Tomaru & Takahashi 2018). Thus, we set the upper limit of the integral at 100 keV. The uncertainty in $T_{\rm IC}$ is propagated via a Monte Carlo technique from errors in the best-fitting spectral model parameters (see details in Clavel et al. 2016), inner disc radius ($R_{\rm in}$; see Section 2.2.2 and Marcel et al. 2019), and our chosen distributions for the binary orbital parameters of BH mass and binary mass ratio (see Table 2 and the following Section). In addition, an absolute minimum for $T_{\rm IC}$ is also applied in this method, whereby $T_{\rm IC}$ will not be sampled below $(T_{\rm IC}/10^8\,{\rm K}) = 0.06kT_{\rm in}$, the absolute minimum $T_{\rm IC}$ for a pure disc blackbody spectrum.

Note that, while the above method works well for the simple power-law spectrum of the hard state, the complex (combination

[1] http://maxi.riken.jp/top/
[2] http://www.swift.ac.uk/user_objects/index.php
[3] This tool provides accretion state information on daily time-scales during outbursts of the population of BH-LMXBs in our Galaxy.
[4] However, also see Marcel et al. 2020 (in preparation) for a thorough discussion on how accretion efficiency may vary in a more complex way during BHXB outburst cycles.
[5] http://svo2.cab.inta-csic.es/theory/fps/
[6] Note that, in the case of the 2009–2011 outburst, the soft state spectral data was re-fitted, allowing the photon index parameter (Γ) to only be sampled in the 2–2.5 interval. This was done to limit the wide dispersion in Γ initially obtained in the soft state spectral fits of this outburst by Clavel et al. (2016).

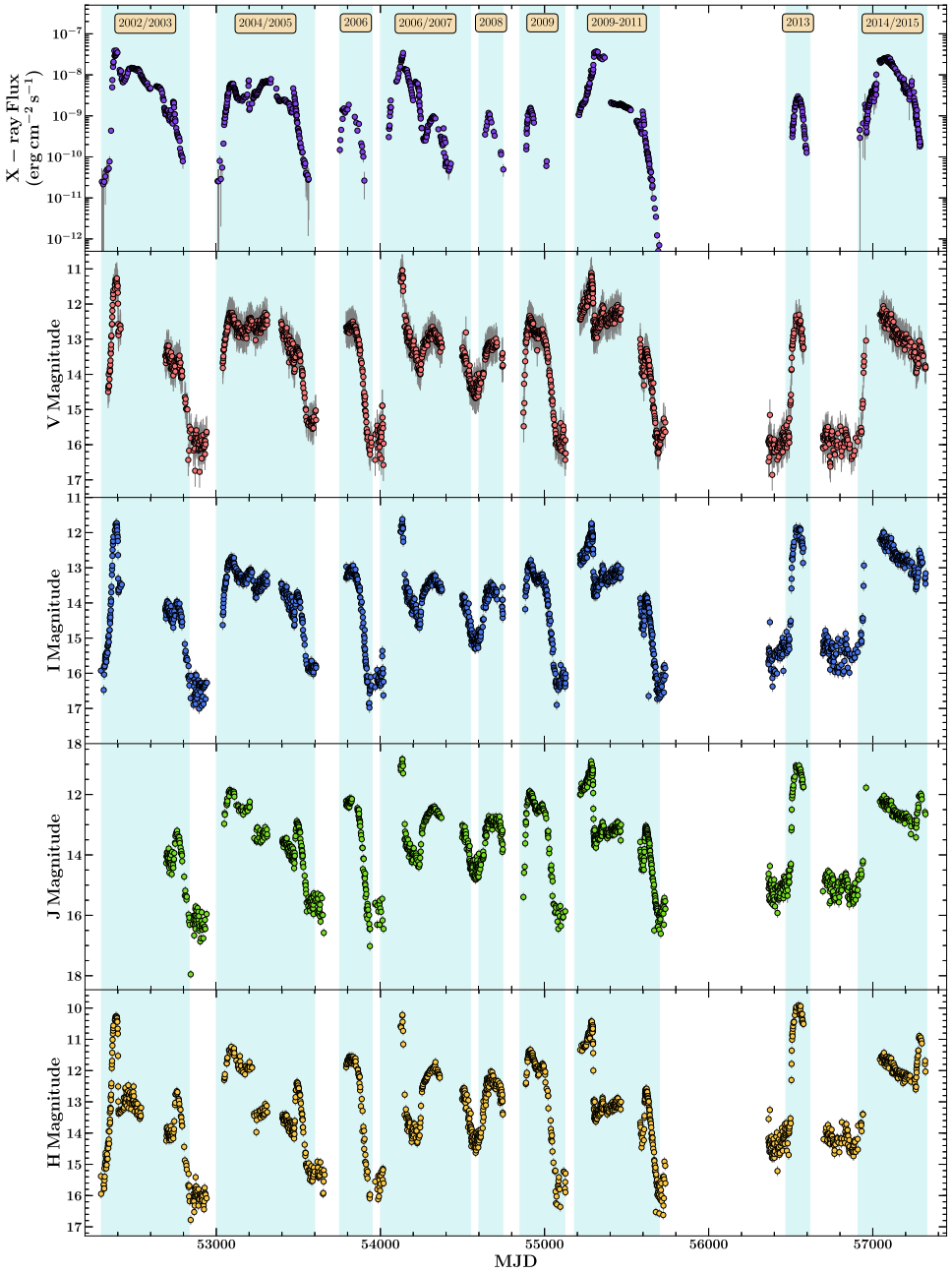

Figure 1. Multiwavelength light curve of GX339–4 between 2002 and 2015. X-ray flux is a combination of *RXTE*/PCA, *Swift*/XRT, and *MAXI*/GSC data (see Section 2.1.1 for details). All OIR data are from SMARTS/ANDICAM and has been dereddened. Shaded cyan regions are meant to guide the eye, marking individual outbursts. See Table 1 for the definition of individual outbursts.

Table 2. Binary orbital parameters used for GX339–4.

BH mass M_1 ($M_\odot$)	Mass ratio ($q = M_2/M_1$)	Orbital period $P_{\rm orb}$ (h)	Distance D (kpc)	$R_{\rm g}$ (cm)	$R_{\rm circ}$ ($\times 10^{10}$ cm)	R_1 ($\times 10^{10}$ cm)	$R_{\rm out}$ ($\times 10^{10}$ cm)
$N(7.8, 1.2)$	$U(0.024, 0.45)$	42.1	8 ± 2	$\left(1.15^{+0.17}_{-0.19}\right) \times 10^6$	$\left(26.62^{+1.42}_{-1.45}\right)$	$\left(63.01^{+3.35}_{-3.43}\right)$	$\left(44.34^{+12.64}_{-12.93}\right)$

disc + power law) spectra existing during the intermediate and soft states must be handled more carefully. The steeper power-law component here tends to dominate the low-energy spectral region in an non-physical way, causing an artificially low estimate for $T_{\rm IC}$. To combat this problem, for intermediate and soft state observations, we take the power-law spectral component to start from the $E_{\rm min} = kT_{\rm in}$ keV, rather than $E_{\rm min} = 0.1$ keV, in the above integral.

Lastly, we note that our estimates for $T_{\rm IC}$ in the soft state, derived using this method, are typically cooler than those estimated by Shidatsu & Done (2019) for the Galactic BHXB H1743–322 (which

based on outburst frequency, is thought to have a similar disc size to GX339–4). However, the soft state spectra of BHXBs tend to be much softer for face-on discs (gravitational redshift dominates) than edge-on discs (doppler blueshift dominates) as a result of doppler/general-relativistic effects (e.g. see Muñoz-Darias et al. 2013). Thus, this is likely only an inclination effect.

2.2 Binary system characteristics

2.2.1 Orbital parameters

While the mass function, orbital period ($P_{\rm orb} = 42.1$ hrs; Hynes et al. 2003; Heida et al. 2017), and stellar companion (K-type star based on detected absorption lines in the near-IR spectrum; Heida et al. 2017), are known in GX339–4, no dynamical mass estimate or constrained estimate for mass ratio currently exists. Thus, we instead follow the procedure of Tetarenko et al. (2018a), and sample these quantities from the Galactic distributions of Özel et al. (2010) and Tetarenko et al. (2016), respectively.

The distance to the source is still a matter of debate. Hynes et al. (2004) suggest GX339–4 is located beyond the Galactic tangent point (giving a lower limit of >6 kpc) based on optical spectra. This is consistent with the recent work of Heida et al. (2017), who derive a conservative lower limit of >5 kpc based on near-IR spectra. Zdziarski et al. (2004) on the other hand, prefer GX339–4 to be located in the Galactic bulge, estimating $D = 8 \pm 2$ kpc based on OIR data. We adopt the distance estimate from Zdziarski et al. (2004) in this work.

Lastly, no estimate of binary inclination for GX339–4 (via ellipsoidal variations) currently exists (although, see Section 5.2.1 for a detailed discussion on this topic). Thus, we do not take into account inclination effects in this analysis. Instead, we average over all angles when computing the disc optical flux (equation A4). See Table 2 for a summary of orbital parameters used in this work.

2.2.2 Evolution of the inner disc radius

To define how $R_{\rm in}$ varies as a function of time during outbursts of GX339–4, we make use of two individual prescriptions (as described below) that employ very different methods. The first relies on modelling the reflection component in X-ray spectra, while the second models the continuum.

The first prescription adopts the $R_{\rm in}$ estimated from X-ray reflection spectroscopy (García et al. 2015; Wang-Ji et al. 2018). These authors provide estimates of $R_{\rm in}$ for multiple hard state observations, taken during the 2002–2003, 2009–2011, 2013, and 2014–2015 outbursts of GX339–4, covering a luminosity range of $\sim 0.6 - 23$ per cent $L_{\rm edd}$ (assuming $M_1 = N(7.8, 1.2)\,{\rm M}_\odot$; Özel et al. 2010). Using these results, we create a linearly interpolated function $R_{\rm in}(\dot{M}_{\rm in}/\dot{M}_{\rm edd})$, valid during the hard accretion state. To create the time-series evolution of $R_{\rm in}$ required for the methodology described in Section 3 and Appendix A, we start by parsing through an individual outburst of GX339–4, and use the data from the WATCHDOG project's Accretion-State-By-Day tool (Tetarenko et al. 2016) to determine the accretion state evolution of the source. If the source is in the hard or intermediate states, we use our interpolated function, along with the observed $\dot{M}_{\rm in}(t)$, to determine $R_{\rm in}(t)$. If the source is in the soft state, we assume $R_{\rm in}(t) = R_g$.

The second prescription uses the unified accretion-ejection paradigm for BH-LMXBs developed by Marcel et al. (2018a,b, 2019). These authors have developed a two-temperature plasma code to effectively model the spectral evolution (at X-ray and radio wavelengths) of BH-LMXB outbursts. They model the observed spectral evolution in a BH-LMXB as the interplay between two different regions of the accretion flow, an inner (jet-emitting) disc (JED) and an outer (standard) accretion disc (SAD),[7] that ultimately leads to changes in $\dot{M}_{\rm in}$ and the transition radius between two disc regions (i.e. $R_{\rm in}$) over an entire outburst cycle. By applying this method to *RXTE*/PCA data of GX339–4 (see e.g. Marcel et al. 2019), they have been able to obtain the time-series evolution of $\dot{M}_{\rm in}(t)$ and $R_{\rm in}(t)$, during outbursts of GX339–4 occurring between 2002 and 2012,[8] which, together uniquely reproduce the X-ray (i.e. $\dot{M}_{\rm in}$ evolution) and (9 GHz) radio light curves of, and evolution of the spectral shape during, each outburst cycle.

3 CONSTRAINING THE X-RAY IRRADIATION OF BHXB ACCRETION DISCS WITH OBSERVATIONS

3.1 The methodology

By directly comparing BH-LMXB outburst light curves at optical and X-ray wavelengths, one can, in principle, track how properties of the X-ray irradiation heating the discs in these systems evolve over time. While the X-ray light curve provides a measure of the bolometric luminosity in these systems, and thus a straightforward means to estimate the central mass-accretion rate on to the BH ($\dot{M}_{\rm in}$; see Section 2.1.1), the optical light curve gives a direct measure of irradiation flux (under the assumption that reprocessing is the dominant source of emission in the optical regime; see Section 3.2 for discussion). Thus, building a relationship between the central mass-accretion rate ($\dot{M}_{\rm in}$) and absolute magnitude in the optical bandpasses, valid during BH-LMXB outbursts, would allow one to place constraints on the fraction of X-ray emission needed to be $\mathcal{C}$ to explain the observed optical flux, and how this fraction changes over a complete outburst cycle.

While the full details of this methodology are presented in Appendix A, the basic idea is as follows: The absolute magnitude, in a particular bandpass, depends only on $\dot{M}_{\rm in}$, BH mass, disc size, and the fraction of X-rays intercepted and $\mathcal{C}$. Thus, by assuming: (i) a constant outer disc radius ($R_{\rm out}$) during outburst, (ii) an inner disc radius that varies as a function of central mass-accretion rate [$R_{\rm in}(\dot{M}_{\rm in})$; see Section 2.2.2], and (iii) a disc temperature profile that is a combination of viscous (Frank, King & Raine 2002),

$$T^4_{\rm visc} = \frac{3GM_1\dot{M}}{8\pi\sigma R^3}\left[1 - \left(\frac{R_{\rm in}}{R}\right)^{1/2}\right], \tag{3}$$

and irradiated (Dubus et al. 1999),

$$T^4_{\rm irr} = \mathcal{C}\frac{\dot{M}c^2}{4\pi\sigma R^2}, \tag{4}$$

portions such that,

$$T^4_{\rm eff}(R) = T^4_{\rm visc}(R) + T^4_{\rm irr}(R), \tag{5}$$

[7]The JED-SAD hybrid disc configuration involves (i) a geometrically thin, optically thick accretion disc extending down to the truncation radius, where (ii) a hot jet emitting disc (JED), threaded by a large-scale vertical magnetic field transporting angular momentum vertically, exists down to the innermost stable circular orbit (ISCO). See Ferreira et al. (2006) and Marcel et al. (2018a,b, 2019) for details.

[8]Note that the 2009–2011 outburst results have already been published in Marcel et al. (2019). Results from the outbursts occurring between 2002 and 2009 will be published in a later paper Gandhi et al. (2010).

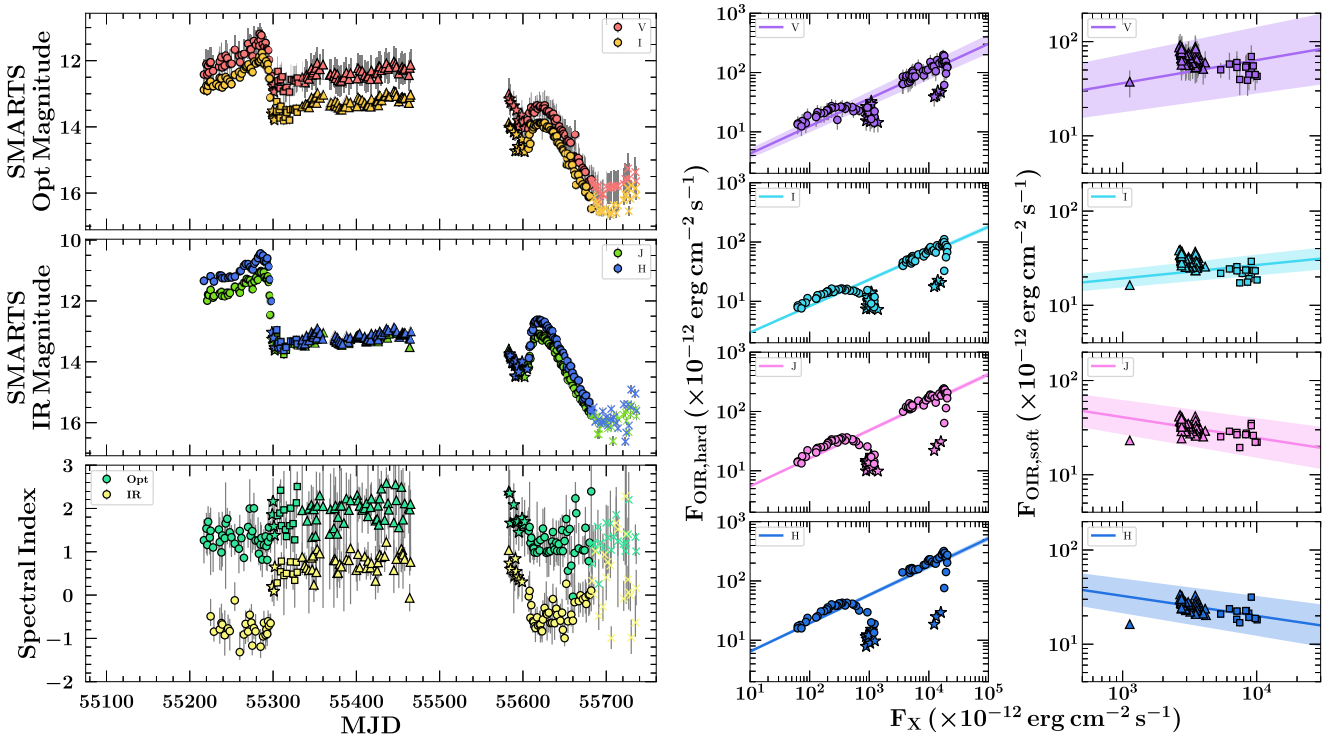

Figure 2. Analysis of the OIR emission processes during the 2009–2011 outburst of GX339–4. Left-hand panel: dereddened SMARTS/ANDICAM light curves in the (top) *V* and *I*, and (middle) *J* and *H*, bands. Optical (*V* and *I*) and IR (*J* and *H*) spectral index (bottom), as a function of time. Middle panel: OIR–X-ray correlations for the hard (and hard-intermediate) accretion states in the *V*-Band (top), *I*-Band (second), *J*-Band (third), and *H*-Band (bottom). Right-hand panel: OIR–X-ray correlations for the soft (and soft-intermediate) accretion states, in the *V*-Band (top), *I*-Band (second), *J*-Band (third), and *H*-Band (bottom). The bolometric (3–200 keV) flux, computed from all available *RXTE*/PCA spectra (see Section 2.1.3 and Marcel et al. 2019 for details on the spectral fitting and analysis), is used as the X-ray data in all correlations. The shapes of the data points in all panels indicate the accretion state of the source as defined by Marcel et al.. Shapes are defined as follows: hard (circles), hard-intermediate (stars), soft (triangles), soft-intermediate (squares), and quiescence (X's). The best-fitting power-law function (solid coloured lines), and 1 σ confidence interval (coloured shaded regions) on the fit, are displayed in each correlation plot.

one can use numerical integration techniques to reconstruct $\mathcal{C}$ from an optical light curve, given the estimate of $\dot{M}_{\rm in}$ derived from a simultaneous X-ray light curve.

3.2 Origin of the OIR emission

In addition to reprocessed X-rays from the outer disc, OIR emission during BH-LMXB outbursts may also be produced by: (i) synchrotron emission from particles accelerated to very high energies (i.e. Lorentz factors of $\gamma \sim 10^6$) in the collimated jets (Homan et al. 2005; Russell et al. 2006), and (ii) hot spots, created as a result of the accretion stream impacting the disc (see Maccarone 2014 and references therein). As such, estimating the contribution of, and correcting for, these two emission mechanisms in the OIR light curves is essential to accurately derive how properties of the X-ray irradiation heating the disc in this system evolve with time (see Section 4 for details).

3.2.1 Tracking the contributions of the disc and jet

BH-LMXB jets produce a broad-band spectrum ($F_\nu \propto \nu^\gamma$ for spectral index γ) characterized by a flat to slightly inverted, optically thick component ($\gamma \gtrsim 0$; Blandford & Königl 1979; Falcke & Biermann 1995; Fender 2001) extending from the radio through OIR wavelengths (Corbel & Fender 2002; Homan et al. 2005; Russell et al. 2006; Chaty, Dubus & Raichoor 2011), that breaks to a steep, optically thin component ($-0.7 < \gamma < -0.5$; Russell et al. 2013).

In contrast, for an accretion disc with a temperature profile of the form, $T(R) \propto R^{-n}$, an optical spectral index of $\gamma = 3–2/n$ is expected in the spectral band corresponding to the summed multicolour disc blackbody. Hence, $\gamma = 1/3$ is expected for a viscous disc ($n = 3/4$). While a γ ranging between $-5/3$ (irradiated isothermal disc following Cunningham 1976 and V90; $n = 3/7$) and -1 (irradiated disc with $n = 1/2$) would correspond to an irradiated disc. If the IR emission was purely from a disc (viscous or irradiated), this would correspond to the Rayleigh–Jeans regime, and thus a $\gamma = 2$ (Frank et al. 2002).

See Hynes et al. (2002) and Hynes (2005) for a discussion on the temperature profile, and corresponding spectral energy distributions (SEDs), of LMXB accretion discs.

As the jet spectrum significantly differs from that of an accretion disc, tracking the changes in the (optical and IR) spectral index over time can be used to understand how the OIR contribution of the disc and jet vary throughout BH-LMXB outbursts. We use a Bayesian Markov chain Monte Carlo (MCMC) algorithm to compute both the optical (using *V* and *I* band data) and IR (using *J* and *H* band data) spectral indexes, along with corresponding 1 σ error bars. The details of this algorithm are explained in Section 3.2.2. The left-hand panels of Fig. 2 plot a combination of the (i) OIR light curve in the *V*, *I*, *J*, and *H* bands, and (ii) the optical (*V* and *I* bands) and IR

Table 3. Disc bright spot contributions in the OIR regime.

Outburst Year	$m_{\rm spot}$ in SMARTS/ANDICAM bands			
	V	I	J	H
2002–2003	$15.6^{+1.7}_{-1.1}$	$15.7^{+1.8}_{-1.1}$	$16.0^{+1.6}_{-1.1}$	$15.9^{+1.6}_{-1.2}$
2004–2005	$16.1^{+1.7}_{-1.0}$	$16.1^{+1.7}_{-1.1}$	$16.5^{+1.8}_{-1.2}$	$16.4^{+1.7}_{-1.2}$
2006	$18.2^{+1.8}_{-1.3}$	$18.3^{+1.7}_{-1.2}$	$18.5^{+1.6}_{-1.2}$	$18.3^{+1.6}_{-1.2}$
2006–2007	$15.7^{+1.6}_{-1.1}$	$15.8^{+1.7}_{-1.1}$	$16.0^{+1.6}_{-1.1}$	$15.8^{+1.7}_{-1.1}$
2008	$18.7^{+1.6}_{-1.1}$	$18.8^{+1.6}_{-1.1}$	$18.9^{+1.9}_{-1.2}$	$18.8^{+1.7}_{-1.2}$
2009	$18.5^{+1.8}_{-1.2}$	$18.6^{+1.7}_{-1.1}$	$18.8^{+1.7}_{-1.1}$	$18.6^{+1.7}_{-1.1}$
2009–2011	$15.6^{+1.8}_{-1.1}$	$15.7^{+1.7}_{-1.1}$	$16.0^{+1.6}_{-1.2}$	$15.8^{+1.8}_{-1.2}$
2013	$18.8^{+1.7}_{-1.1}$	$19.0^{+1.6}_{-1.1}$	$19.1^{+1.7}_{-1.1}$	$19.0^{+1.8}_{-1.1}$
2014–2015	$15.8^{+1.7}_{-1.0}$	$15.9^{+1.7}_{-1.1}$	$16.1^{+1.8}_{-1.0}$	$16.0^{+1.6}_{-1.1}$

(J and H bands) spectral indexes, used to determine which emission process dominates during the 2009–2011 outburst of GX339–4, as a function of time and X-ray accretion state. Figs B1–B4 in Appendix B show these results for the remaining eight outbursts in our sample.

Bright spots in X-ray binaries are difficult to detect. To actually detect these bright spots, the X-ray binary would have to be: (i) in quiescence, where $\dot{M}_t$ into the outer disc $\gg \dot{M}_{\rm in}$ on to the BH, or (ii) in the radiatively inefficient accretion regime during outburst (i.e. early rise and late decay), where $\dot{M}_{\rm in}$ on to the BH is low (e.g. McClintock, Horne & Remillard 1995; Froning et al. 2011; Maccarone 2014). To compute the theoretical contribution of the bright-spot to the V, I, J, and H bands, we follow the procedure outlined in Dubus, Otulakowska-Hypka & Lasota (2018), assuming a luminosity of the form

$$L_{\rm spot} = \frac{GM\dot{M}_t}{2R_{\rm disc}}\left(1 - \frac{R_{\rm disc}}{R_1}\right), \tag{6}$$

and a temperature of $T_{\rm eff,\,spot} = 15\,000$ K (Groot, Rutten & van Paradijs 2001). Here, we estimate the mass transfer rate from the companion ($\dot{M}_t$) by calculating the time-averaged $\dot{M}_{\rm in}$ over each outburst (see Tetarenko et al. 2016 for details on this method). This takes into account that the mass transfer rate from the companion may be increased during outburst from its time-averaged value over several outbursts. Thus, the estimated $\dot{M}_t$ is an upper limit to the average mass transfer. Uncertainties in $\dot{M}_{\rm in}$, M_1, q, D, and V-band magnitude (i.e. instrument uncertainty and error in interstellar reddening), are all taken into account when computing the bright-spot contribution and its uncertainty (see Table 3). Comparing to the magnitudes in Fig. 1 confirms that the hotspot OIR contribution is small in outburst.

3.2.2 *Quantifying the jet contribution*

Another instrumental tool we can use to study the emission processes in BH-LMXBs is the observed correlation between OIR flux and X-ray flux during outburst. In a study of 33 LMXBs, Russell et al. (2006) found individual global power-law correlations ($F_{\rm OIR} = N_{\rm pl} F_X^{\beta}$) valid during the hard and soft accretion states. The specific slope (β) of these correlations is expected to vary depending on the dominant emission mechanism (van Paradijs & McClintock 1994; Hynes 2005; Russell et al. 2006; Coriat et al. 2009). Thus, fitting power-law correlations to observed outburst data can help one determine the dominant emission mechanisms present, and also verify conclusions made from the multiwavelength SEDs, as discussed above.

If the disc temperature varies as $T = T_0(R/R_0)^{-n}$ with $T_0 \propto \dot{M}^m$, then the flux in the multicolour disc blackbody varies like $F_{\rm disc} \propto \dot{M}^{2m/n}$ while $F_{\rm RJ} \sim \dot{M}^m$ in the Rayleigh–Jeans (RJ) tail. The X-ray flux F_X is either $\propto \dot{M}$ (soft state) or $\dot{M}^2$ (hard state) depending on radiative efficiency (see Section 2.1.1).

For a viscously heated disc ($m = 1/4$, $n = 3/4$), the expected slope ranges from $\beta = 0.13$ (RJ) to $\beta = 0.33$ (disc) in the hard state, $0.26 \leq \beta \leq 0.67$ in the soft state. For X-ray reprocessing with an isothermal disc ($m = 2/7$, $n = 3/7$), the slope ranges between $0.14 \leq \beta \leq 0.67$ in the hard state, $0.28 \leq \beta \leq 1.33$ in the soft state. The OIR flux is usually at the spectral transition between the RJ tail and the multicolour blackbody, given the outer disc temperature of 10 000 K in outburst (Russell et al. 2006). In contrast, under the assumption that the optically thick jet spectrum is flat from the radio through OIR regimes, a slope of $\beta \sim 0.7$ is expected in the optical and IR regime (Corbel et al. 2003; Gallo, Fender & Pooley 2003; Russell et al. 2006).

As BH-LMXB jets are typically only observed in the hard state, they should contribute a negligible amount of OIR flux in the soft state. Thus, one can estimate the fraction of the total OIR flux (in a given bandpass) that comes from the jet versus the disc by computing the difference between the offset of hard and soft state data (i.e, comparing the power-law normalization parameters, $N_{\rm pl}$, of the hard and soft state correlations fits). See Russell et al. (2006) for a detailed description and application of this method to a large sample of LMXBs.

First, we use a Bayesian MCMC algorithm (Foreman-Mackey et al. 2013) to perform a linear fit in log space, and estimate the slope (s_ν) and intercept (b_ν), for each individual correlation. To properly take into account uncertainties in both OIR flux (propagated from instrument and interstellar reddening errors) and X-ray flux,[9] we use an alternative method to the standard linear formulation (i.e. $y = s_\nu x + b_\nu$). This method parametrizes the fit in terms of the θ parameter, defined as the angle that the linear function makes with the x-axis, and the y-intercept, y_b (Hogg, Bovy & Lang 2010). After likelihood maximization, posterior probability distributions (PDFs) of s_ν and b_ν are obtained by taking the tangent of the PDFs of (θ, y_b). See Shaw et al. (2019) for details on this fitting algorithm. Secondly, we compute the hard state jet contribution to the V, I, J, and H bandpasses using the best-fitting power-law normalization parameters ($N_{\rm pl} = 10^{b_\nu}$) of the hard and soft state OIR-correlations. In this method, uncertainty in D and V-band magnitude (a combination of instrument uncertainty and interstellar reddening errors) is taken into account when computing the jet contribution and its uncertainty. See Table 4, for jet contributions in each waveband, Fig. 4, which shows select OIR SEDs, taken during the 2009-2011 outburst, before and after the OIR data were corrected for the jet contribution, and Table 5, which displays the best-fitting parameters (s_ν, b_ν) for each correlation.

The middle and right-hand panels of Fig. 2 plot the OIR–X-ray correlations in the V, I, J, and H bands, for each individual accretion state, used to estimate the contributions of the jet at OIR wavelengths during the 2009–2011 outburst of GX339–4, as a function of X-ray accretion state and X-ray flux. The β index is compatible with multicolour disc blackbody emission in the soft state, either from an irradiated or non-irradiated disc. The values of β in the hard state

[9]The bolometric (3–200 keV) flux used here has been computed by fitting all available *RXTE*/PCA spectra with a two-component disc blackbody plus power-law model. See Section 2.1.3 and Marcel et al. 2019 for details on the spectral fitting and analysis.

Table 4. Jet contributions in the OIR regime.

Outburst Year	$F_{\rm jet}/F_{\rm tot}$ in SMARTS/ANDICAM bands V	I	J	H
2002–2003	$0.41^{+0.08}_{-0.09}$	–	$0.99^{+0.0002}_{-0.0001}$	–
2004–2005	$0.38^{+0.12}_{-0.07}$	–	–	$0.56^{+0.01}_{-0.02}$
2006–2007	$0.60^{+0.03}_{-0.04}$	$0.37^{+0.02}_{-0.03}$	$0.40^{+0.02}_{-0.03}$	$0.73^{+0.01}_{-0.01}$
2009–2011	$0.81^{+0.01}_{-0.01}$	$0.84^{+0.001}_{-0.002}$	$0.99^{+0.00002}_{-0.00003}$	$0.99^{+0.00005}_{-0.00006}$
2014–2015	$0.81^{+0.11}_{-0.06}$	$0.94^{+0.003}_{-0.002}$	$0.98^{+0.0007}_{-0.0006}$	$0.99^{+0.0001}_{-0.0002}$

The jet contribution cannot be estimated for the 'failed' outbursts of GX339–4 (2006, 2008, 2009, and 2013), since there is no soft state data to draw from.

are higher than in the soft state, and higher than expected from disc emission, supporting a significant contribution from the jet to the OIR emission. Figs B1–B4 in Appendix B show these results for the remaining eight outbursts in our sample.

4 RESULTS

4.1 The time series evolution of the X-ray irradiating source in GX339–4

We have applied the methodology, briefly summarized in Section 3 and thoroughly described in Appendix A, to the X-ray (*RXTE*/PCA, *Swift*/XRT, and *MAXI*/GSC) and jet/bright-spot corrected optical (SMARTS/ANDICAM) data available for GX339–4 (see Section 2.1 and Table 1). In doing so, we have derived: (i) how the fraction of X-ray intercepted and reprocessed in the outer disc evolves with time, $\mathcal{C}(t)$, (ii) how the temperature of the irradiation at the outer disc radius evolves with time, $T_{\rm irr}(R_{\rm out}, t)$, and (iii) placed constraints on the evolution of the inner radius of the optically emitting portion of the disc, $R_{\rm opt,\,in}(t)$, throughout nine individual outburst cycles.

$\mathcal{C}(t)$ is computed, for each time t_i during which simultaneous X-ray and optical data are available, by starting with $\dot{M}_{\rm in}(t)$ (computed from the X-ray light curve; see Section 2.1.1), then varying $\mathcal{C}$ until the observed V-band magnitude is obtained. The confidence interval on $\mathcal{C}(t)$ is propagated by taking into account errors in X-ray flux, D, M_1, q, $R_{\rm in}(t)$, and V-band magnitude (which itself is a combination of instrument uncertainty and error on interstellar reddening). Note that the V-band light curve used here, and thus the derived $\mathcal{C}$, has been corrected for both optical contributions from the jet and the disc bright-spot (see Section 3.2 for details). $T_{\rm irr}(t, R_{\rm out})$ is computed using $\mathcal{C}(t)$ and $\dot{M}_{\rm in}(t)$ in equation (4).

To compute $R_{\rm opt,\,in}(t)$, we start by computing $\dot{M}_{\rm in} - M_V$ relationships for a range of constant $R_{\rm in}$ between R_g and $R_{\rm disc} \sim 4 \times 10^5\,R_g$. Then, for each t_i during which simultaneous X-ray and optical data are available, we truncate the disc in increments of R_g, and compute $\mathcal{C}(t_i\,,\,R/R_g)$ in each case. When the deviation between $\mathcal{C}(t_i\,,\,R_g)$ and $\mathcal{C}(t_i\,,\,R)$ reaches a particular threshold, we take this to indicate that the radius R is within the optical emitting region of the disc. This procedure is performed for a threshold of 3σ for each outburst. The $R_{\rm opt,\,in}(t)$ we compute with this method can be thought of as a conservative upper limit on the inner radius of the outer, irradiated portion of the disc responsible for the optical emission.

Fig. 3 displays $\mathcal{C}$, $T_{\rm irr}(R_{\rm out})$, and $R_{\rm opt,\,in}$ derived using two different prescriptions for the evolution of $\dot{M}_{\rm in}$ and $R_{\rm in}$ over the 2009–2011 outburst of GX339–4: (i) The observed $\dot{M}_{\rm in}(t)$ computed from the X-ray data and $R_{\rm in}(t)$ interpolated from X-ray reflection spectroscopy results (García et al. 2015; Wang-Ji et al. 2018), and (ii) The $\dot{M}_{\rm in}(t)$, $R_{\rm in}(t)$ derived in Marcel et al. (2018a,b, 2019). See Section 2.1.1 and 2.2.2 for a detailed discussion on each prescription. The results for the remaining eight outbursts in our sample can be found in Figs C1–C4 in Appendix C.

Note that Marcel et al. assume a BH mass for GX339–4 of $M_1 = 5.8\,{\rm M}_\odot$ and do not take into account accretion efficiency when computing $\dot{M}_{\rm in}$. To directly compare to the $\dot{M}_{\rm in}$ computed from the observational X-ray data and the $R_{\rm in}$ interpolated from the Garcia et al. and Wang-Ji et al. estimates using X-ray reflection spectroscopy, we scale the ($\dot{M}_{\rm in}$, $R_{\rm in}$) results from Marcel et al. to a BH mass of $M_1 = N(7.8, 1.2)\,{\rm M}_\odot$, and apply an accretion efficiency (η) as defined in Section 2.1.1.

5 DISCUSSION

The time-series evolution of the fraction of X-rays intercepted and $\mathcal{C}$, that we have derived from the observed X-ray and optical light curves, varies in a complex way during the nine outbursts of GX339–4 in our sample. However, the values of $\mathcal{C}$ do not exceed $\approx 10^{-2}$, in agreement with previous rough estimates of the reprocessed fraction based on the optical to X-ray ratio. This confirms that using breaks in the X-ray light curve to constrain $\mathcal{C}$ is much less reliable and can lead to unphysical values (Tetarenko et al. 2018a).

First, we find that the value of $\mathcal{C}$ in the soft accretion state ($\mathcal{C}_{\rm soft}$) tends to be higher than $\mathcal{C}$ in the hard accretion state ($\mathcal{C}_{\rm hard}$), at least during 'canonical' outbursts (consistent with results from other BH-LMXB sources; see discussion below and Fig. 5). However, we caution that the difference is sensitive to the OIR contribution from the jet and/or cyclosynchrotron emission from the hot flow itself. $\mathcal{C}_{\rm hard}$ during 'failed' outbursts, when no jet contribution can be estimated due to the lack of soft state, is typically comparable to the $\mathcal{C}_{\rm soft}$ 'canonical' outburst values. Thus, the larger values of $\mathcal{C}_{\rm hard}$ during 'failed' outbursts should only be considered upper limits and are likely a consequence of not being able to correct the light curves for an optical jet contribution. For comparison, $\mathcal{C}_{\rm hard}$ rises by a factor $10 - \approx 2 \times 10^{-3}$ for the 2009–2011 outburst if the optical jet contribution is not removed.

Secondly, we find some difference when comparing the values of $\mathcal{C}$ derived using the Marcel et al., Garcia et al., and Wang et al. prescriptions (e.g. see Table 6). Of the seven outbursts for which we have estimated $\mathcal{C}$ using both prescriptions, typically the $\mathcal{C}$ derived using Marcel et al. are smaller, when compared to the Garcia et al. and Wang et al. prescription results for the same outburst. This difference is entirely the result of their different estimates for $\dot{M}_{\rm in}$. Their very different assumptions for $R_{\rm in}$ have no effect whatsoever for this as the innermost radius of the disc which contributes substantially to the optical emission, $R_{\rm opt,\,in}$ (see Fig. 3 and Appendix C) is around $10^5 R_g$, much larger than even the largest estimate of the truncation of the thin disc ($R_{\rm in} \ll 10^3 R_g$) in Marcel et al..

Thirdly, we observe peaks/drops in $\mathcal{C}$ coinciding with both hard–soft and soft–hard state transitions. Given that $R_{\rm in} \ll R_{\rm opt,\,in}$ throughout all outbursts in our sample (as discussed above), it is clear that these abrupt changes in $\mathcal{C}$ are not simply a consequence of $R_{\rm in}$ changing suddenly during the outburst.

Evidence for this type of behaviour has been (i) to an extent, observed previously in BH-LMXBs XTEJ1817–330 and XTEJ1859+226, and (ii) recently predicted by Dubus et al. (2019), who consider the impact a thermally driven wind would have on BH-LMXB light curves, in the context of the disc-instability model. By fitting an irradiated disc model to broad-band SEDs observed throughout the 2006 outburst of XTE J1817–330, Gierliński et al. (2009) found that while soft state observations were consistent

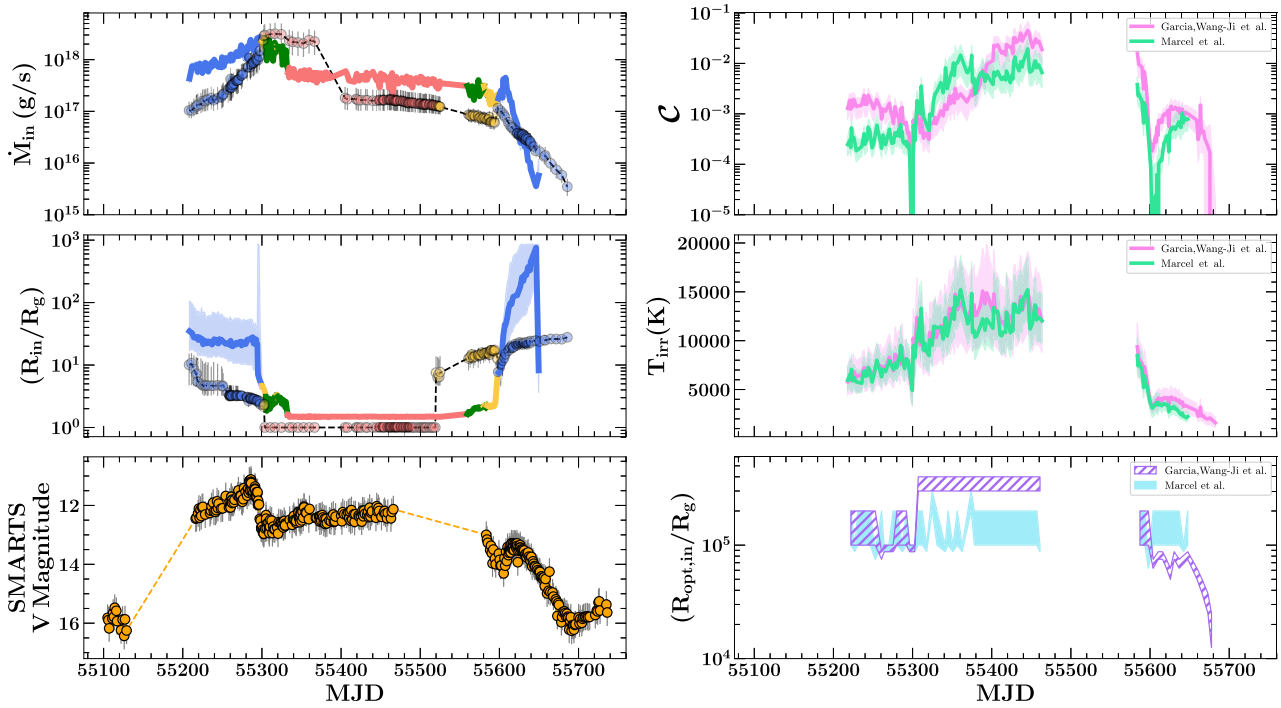

Figure 3. The 2009–2011 outburst of GX339–4. Left-hand panel: (top) Central mass-accretion rate ($\dot{M}_{\rm in}$), (middle) inner disc radius ($R_{\rm in}$) in units of R_g [for $M_1 = N(7.8, 1.2)\,{\rm M}_\odot$], and (bottom) dereddened SMARTS/ANDICAM V-band magnitude, as a function of time. In the top and middle panels: (i) The translucent data points correspond to the $\dot{M}_{\rm in}$ calculated from the X-ray data and $R_{\rm in}$ interpolated from the Garcia et al. and Wang-Ji et al. estimates using X-ray reflection spectroscopy, respectively. The solid lines are output from the Marcel et al. analysis. Both data points and solid lines are colour coded by accretion state. The colours of the data points and solid lines correspond to accretion state estimates from the WATCHDOG Project's Accretion-State-By-Day tool, and the accretion state definitions from Marcel et al., respectively. The colours are defined as follows: red (soft state), yellow (intermediate state; referred to as hard-intermediate state in Marcel et al.), blue (hard state), and green (soft intermediate state; Marcel et al. only). Uncertainties on the data points (represented as grey error bars) are propagated from errors in X-ray flux, distance, and BH mass. The coloured shaded regions show the uncertainties in ($\dot{M}_{\rm in}$, $R_{\rm in}$) derived in Marcel et al. (2019). The black (top and middle) and orange (bottom) dashed lines are only meant to guide the eye. Right-hand panel: (top) The fraction of X-rays intercepted and $\mathcal{C}$ as a function of time, calculated using: the $\dot{M}_{\rm in}$ computed from the X-ray data and the $R_{\rm in}$ interpolated from the Garcia et al. and Wang-Ji et al. estimates using X-ray reflection spectroscopy, and the output of the Marcel et al. analysis. Coloured shaded regions show the 1σ confidence interval on $\mathcal{C}$, computed by taking into account uncertainty in X-ray flux, distance, BH mass, binary mass ratio, inner disc radius, and V-band magnitude. (Middle) The irradiation temperature at the outer disc radius, $T_{\rm irr}(R_{\rm out})$, as a function of time. See Section 4.1 for details. Coloured shaded regions represent the 1σ confidence interval on $T_{\rm irr}(R_{\rm out})$. (bottom) The inner radius of the optically emitting portion of the disc ($R_{\rm opt,\,in}$) as a function of time. $R_{\rm opt,\,in}$ is calculated using the two different prescriptions for $\mathcal{C}$ (see above) and considering a 3σ deviation in $\mathcal{C}$ (see Section 4.1 for details). Note that optical V-band contributions from the disc bright-spot and jet have been corrected for when computing $\mathcal{C}(t)$, $T_{\rm irr}(R_{\rm out})$, and $R_{\rm opt,\,in}(t)$. See Section 3.2 for discussion.

with a near constant fraction of bolometric X-ray luminosity being $\mathcal{C}$, the reprocessed fraction increased by a factor $\sim$6 as the source transitioned into the hard state. These authors suggest that their observations favour direct illumination of the outer disc by the central X-ray source, and explain the apparent increase in reprocessed fraction as the source transitions to the hard state as a consequence of a change in disc albedo during the state transition, though they did not model this in detail. Note, however, that this study did not take into account the jet contribution in the optical as we do in this paper.

Similarly, through broad-band SED modelling during the 1999–2000 outburst of XTEJ1859+226, Kimura & Done (2019) find evidence for a decrease in the reprocessed fraction as the source dims from the soft state towards (but not quite reaching) the hard state. Unlike Gierliński et al. (2009), these authors did calculate the expected reprocessed fraction from direct illumination, and found that it was smaller than required. They suggested another source of irradiation of the outer disc, in addition to direct illumination. Kimura & Done (2019) consider the idea, originally suggested by Begelman, McKee & Shields (1983), that the disc could also be irradiated by a corona/wind existing above the disc, by effectively scattering a portion of the central X-ray luminosity back on to the outer disc. They estimated the strength of the wind irradiation as being similar to that required by the data. Fig. 4 shows a comparison of this SED fitting method in XTEJ1859+226 with some of our data for GX339–4. We fit the soft state SED with the OPTXRPLIR model for BH mass of $7.8\,{\rm M}_\odot$, distance of 8 kpc, $R_{\rm out} = 10^{5.4}\,R_g$, and inclination of 30° with $\mathcal{C} \approx 2 \times 10^{-3}$, similar to that derived for XTEJ1859+226 and rather smaller than the value $\mathcal{C} \approx 7 \times 10^{-3}$ derived on the same date by our method with the Marcel et al. analysis (see Fig. 3). However, their exists a number of additional biases that may be affecting our determination of $\mathcal{C}$ (up to a factor 3–5), comparable to the systematic uncertainty in our method (see Appendix A), most importantly from inclination. Changing the inclination to 60° (as assumed by using the angle average disc flux) increases $\mathcal{C} \approx 10^{-2}$.

Fig. 4 also shows that the soft state V-band flux is somewhat higher than the OPTXRPLIR model fit to the H, J, I data. This could indicate that the reddening correction is overestimated as even a single temperature blackbody underestimates the V-band flux. Our

Table 5. OIR–X-ray correlation best fits.

Outburst ID	OIR Band	Hard state s_ν	Hard state b_ν	Soft state s_ν	Soft state b_ν
2002–2003	*V*	$0.37^{+0.01}_{-0.02}$	$0.37^{+0.05}_{-0.06}$	$0.27^{+0.07}_{-0.08}$	$0.60^{+0.24}_{-0.25}$
	I	$0.39^{+0.005}_{-0.004}$	$0.09^{+0.01}_{-0.01}$	$0.26^{+0.01}_{-0.02}$	$0.31^{+0.07}_{-0.06}$
	J	$0.25^{+0.02}_{-0.01}$	$0.59^{+0.02}_{-0.03}$	$-0.39^{+0.09}_{-0.08}$	$2.26^{+0.23}_{-0.27}$
	H	$0.48^{+0.005}_{-0.004}$	$0.16^{+0.02}_{-0.01}$	$0.38^{+0.02}_{-0.01}$	$-0.03^{+0.05}_{-0.04}$
2004–2005	*V*	$0.41^{+0.02}_{-0.01}$	$0.25^{+0.04}_{-0.04}$	$0.73^{+0.06}_{-0.09}$	$-0.79^{+0.29}_{-0.18}$
	I	$0.40^{+0.003}_{-0.004}$	$0.07^{+0.01}_{-0.01}$	$0.37^{+0.03}_{-0.02}$	$0.06^{+0.07}_{-0.08}$
	J	$0.47^{+0.004}_{-0.005}$	$0.15^{+0.02}_{-0.01}$	$0.30^{+0.04}_{-0.03}$	$0.38^{+0.09}_{-0.08}$
	H	$0.49^{+0.006}_{-0.005}$	$0.17^{+0.02}_{-0.01}$	$0.21^{+0.04}_{-0.03}$	$0.58^{+0.08}_{-0.09}$
2006	*V*	$0.50^{+0.01}_{-0.02}$	$0.07^{+0.04}_{-0.05}$	–	–
	I	$0.51^{+0.01}_{-0.01}$	$-0.14^{+0.02}_{-0.01}$	–	–
	J	$0.67^{+0.01}_{-0.01}$	$-0.17^{+0.01}_{-0.02}$	–	–
	H	$0.65^{+0.01}_{-0.01}$	$-0.12^{+0.03}_{-0.02}$	–	–
2006–2007	*V*	$0.59^{+0.01}_{-0.02}$	$-0.36^{+0.07}_{-0.06}$	$0.30^{+0.07}_{-0.06}$	$0.47^{+0.21}_{-0.27}$
	I	$0.55^{+0.02}_{-0.01}$	$-0.40^{+0.01}_{-0.02}$	$0.25^{+0.03}_{-0.02}$	$0.30^{+0.07}_{-0.06}$
	J	$0.61^{+0.01}_{-0.01}$	$-0.27^{+0.01}_{-0.02}$	$0.25^{+0.03}_{-0.02}$	$0.34^{+0.08}_{-0.07}$
	H	$0.65^{+0.01}_{-0.01}$	$-0.29^{+0.03}_{-0.02}$	$0.16^{+0.03}_{-0.02}$	$0.62^{+0.08}_{-0.07}$
2008	*V*	$0.28^{+0.10}_{-0.09}$	$0.78^{+0.23}_{-0.28}$	–	–
	I	$0.25^{+0.03}_{-0.04}$	$0.62^{+0.10}_{-0.09}$	–	–
	J	$0.45^{+0.04}_{-0.03}$	$0.43^{+0.08}_{-0.09}$	–	–
	H	$0.55^{+0.02}_{-0.03}$	$0.27^{+0.08}_{-0.06}$	–	–
2009	*V*	$0.21^{+0.04}_{-0.05}$	$0.99^{+0.16}_{-0.14}$	–	–
	I	$0.30^{+0.03}_{-0.02}$	$0.49^{+0.09}_{-0.08}$	–	–
	J	$0.36^{+0.03}_{-0.04}$	$0.68^{+0.12}_{-0.13}$	–	–
	H	$0.47^{+0.02}_{-0.03}$	$0.44^{+0.09}_{-0.07}$	–	–
2009–2011	*V*	$0.46^{+0.01}_{-0.02}$	$0.17^{+0.06}_{-0.07}$	$0.25^{+0.05}_{-0.04}$	$0.82^{+0.16}_{-0.17}$
	I	$0.45^{+0.01}_{-0.01}$	$0.03^{+0.01}_{-0.02}$	$0.14^{+0.02}_{-0.01}$	$0.86^{+0.06}_{-0.05}$
	J	$0.47^{+0.01}_{-0.02}$	$0.27^{+0.01}_{-0.02}$	$-0.22^{+0.02}_{-0.03}$	$2.27^{+0.09}_{-0.10}$
	H	$0.48^{+0.01}_{-0.01}$	$0.33^{+0.02}_{-0.02}$	$-0.21^{+0.02}_{-0.03}$	$2.15^{+0.10}_{-0.09}$
2013	*V*	$0.30^{+0.20}_{-0.16}$	$0.72^{+0.46}_{-0.63}$	–	–
	I	$0.34^{+0.05}_{-0.05}$	$0.76^{+0.15}_{-0.16}$	–	–
	J	$0.39^{+0.04}_{-0.05}$	$0.98^{+0.14}_{-0.12}$	–	–
	H	$0.40^{+0.05}_{-0.04}$	$1.32^{+0.13}_{-0.15}$	–	–
2014–2015	*V*	$0.23^{+0.03}_{-0.04}$	$0.72^{+0.11}_{-0.12}$	$2.09^{+0.41}_{-0.72}$	$-7.21^{+3.10}_{-1.74}$
	I	$0.11^{+0.02}_{-0.01}$	$1.23^{+0.04}_{-0.05}$	$0.71^{+0.12}_{-0.13}$	$-1.20^{+0.56}_{-0.52}$
	J	$-0.07^{+0.01}_{-0.02}$	$1.95^{+0.04}_{-0.05}$	$0.77^{+0.12}_{-0.13}$	$-1.48^{+0.55}_{-0.54}$
	H	$-0.23^{+0.02}_{-0.01}$	$2.69^{+0.04}_{-0.03}$	$0.82^{+0.11}_{-0.12}$	$-1.53^{+0.50}_{-0.47}$

Note.–The best-fitting linear function to the data in log space, $\log_{10}(F_{\rm OIR}) = s_\nu \log_{10}(F_X) + b_\nu$ for a slope of s_ν and a *y*-intercept of b_ν, is presented here. For comparison to the standard power-law correlations, $F_{\rm OIR} = N_{\rm pl} F_X^{\beta}$, the slope $\beta = s_\nu$, and the power-law normalization $N_{\rm pl} = 10^{b_\nu}$.

model fits only to the *V*-band flux, so this (along with inclination) would also lead to a larger $\mathcal{C}$. Conversely, the *V*-band data from both the bright and dim low/hard states are well fit by $\mathcal{C} \approx 2 \times 10^{-3}$ for inclination of 30°, which is the origin of the decrease in $\mathcal{C}$ for the low/hard state.

We note also that the OPTXRPLIR model takes into account disc colour corrections due to electron scattering in the disc photosphere. This becomes important when the material is ionized i.e. for UV and X-ray local temperatures, so does not affect the optical spectrum so should not affect the calculation of $\mathcal{C}$, but leads to a shift in the spectrum above 10 eV (see fig. 3 of Kimura & Done 2019).

It is also clear from Fig. 4 that the amount of irradiation is similar in GX339–4 and XTE J1859+226. However, the disc outer radius is larger in GX339–4, which works to extend the region over which irradiation dominates in the disc. XTE J1859+226 has not been re-scaled as the distance estimate used is also 8 kpc. It has a slightly smaller best fit mass of 6.9 $M_\odot$ which is why this spectrum has higher $L/L_{\rm Edd} \sim 0.2$ than the 0.1 for the soft state of GX339–4 shown in Fig. 4.

Dubus et al. (2019) used the analytic estimates of scattering in a thermal-radiative wind to predict the time-series evolution of $\mathcal{C}$, for a number of model BH-LMXB light curves with a range of orbital periods. They find complex variability in $\mathcal{C}$ throughout the outbursts, as the wind responds to changes in luminosity and spectral shape. However, there is always a sudden drop (resp. rise) in $\mathcal{C}$ when going from the hard to soft state (resp. soft to hard). This is due to the sudden change in spectral shape, which makes a sudden change in Compton temperature, so a sudden change in launch radius of the wind (see Done et al. 2018).

Given the observed (i) complex profiles in $\mathcal{C}$, (ii) correlations between $\mathcal{C}$ and accretion state, (iii) variations in $\mathcal{C}$ (sometimes up orders of magnitude) on time-scales of days to weeks, and (iv) the typically large derived values for truncation radius of the optically emitting part of the disc ($R_{\rm opt,\,in} \gtrsim 10^5 R_g$), we first consider a scattering origin for the X-ray irradiation in GX339–4.

5.1 Irradiation heating via a thermally driven wind

We make use of the thermally driven (Compton heated) wind prescription from Done et al. (2018). These authors have combined analytical (Begelman et al. 1983) and numerical (Woods et al. 1996) thermal wind models to predict disc wind observables (e.g. column density, ionization state, mass-loss rates, wind launching radii, and velocity) as a function of changing spectral shape and luminosity ($L_{\rm X}$) throughout outburst. We briefly present the basic idea behind this (Compton heated) thermal wind model below and refer the reader to Begelman et al. (1983), Woods et al. (1996), and Done et al. (2018) for further details on the model and to Kimura & Done (2019) for an example of application of the model to BH-LMXB XTEJ1859+226.

5.1.1 Deriving observational properties of the wind throughout an outburst cycle

During outburst, the surface of the disc is heated to the Compton temperature ($T_{\rm IC}$), which only depends on the X-ray irradiating spectrum. This X-ray irradiation results in the formation of a corona above the disc. The scale height of this corona is controlled by the ratio of sound speed ($c_{\rm IC}^2 = kT_{\rm IC}/\mu$; where μ is mean particle mass) of the gas, to the escape velocity ($v_{\rm esc} \sim GM/R$), in the disc. If $c_{\rm IC} \geq v_{\rm esc}$ the gas will escape in a wind, at a launch radius defined by the Compton radius

$$R_{\rm IC} = \frac{GM_1}{c_{\rm IC}^2} \approx 10^{12} \left(\frac{M_1}{10{\rm M}_\odot}\right) \left(\frac{10^7\,{\rm K}}{T_{\rm IC}}\right) {\rm cm}, \quad (7)$$

where M_1 is the BH mass and $T_{\rm IC}$ is the Compton temperature of the impinging irradiation. Otherwise, the material will form a type of static corona above the disc (Begelman et al. 1983).

Table 6. Correlation between X-ray irradiation, accretion state, and outburst phase.

Outburst ID	Average $\mathcal{C}$	Average $\mathcal{C}$ per accretion state				Average $\mathcal{C}$ per outburst phase		
		Soft state	Hard state	(Hard-)intermediate state	soft-intermediate state	Rise	Plateau	Decay
Prescription 1: $\mathcal{C}$ derived using $\dot{M}_{\rm in}$ computed from observed X-ray light curves and $R_{\rm in}$ estimated from X-ray reflection spectroscopy								
2002–2003	$(1.3 \pm 0.1) \times 10^{-3}$	$(2.7 \pm 0.5) \times 10^{-3}$	$(1.9 \pm 0.2) \times 10^{-3}$	$(8.0 \pm 1.1) \times 10^{-4}$	–	$(3.3 \pm 0.7) \times 10^{-3}$	$(9.5 \pm 1.0) \times 10^{-4}$	$(2.0 \pm 0.2) \times 10^{-3}$
2004–2005	$(2.4 \pm 0.1) \times 10^{-3}$	$(5.4 \pm 0.3) \times 10^{-3}$	$(1.9 \pm 0.1) \times 10^{-3}$	$(5.4 \pm 0.7) \times 10^{-3}$	–	$(4.1 \pm 0.4) \times 10^{-2}$	$(2.1 \pm 0.1) \times 10^{-3}$	$(3.1 \pm 0.3) \times 10^{-3}$
2006	$(1.4 \pm 0.1) \times 10^{-2}$	–	$(1.4 \pm 0.1) \times 10^{-2}$	–	–	–	–	$(1.4 \pm 0.1) \times 10^{-2}$
2006–2007	$(1.5 \pm 0.1) \times 10^{-3}$	$(1.2 \pm 0.1) \times 10^{-3}$	$(1.7 \pm 0.1) \times 10^{-3}$	$(1.0 \pm 0.5) \times 10^{-3}$	–	$(2.5 \pm 0.6) \times 10^{-3}$	$(1.3 \pm 0.1) \times 10^{-3}$	$(3.3 \pm 0.3) \times 10^{-3}$
2008	$(1.1 \pm 0.1) \times 10^{-2}$	–	$(1.1 \pm 0.1) \times 10^{-2}$	–	–	$(9.6 \pm 1.2) \times 10^{-3}$	–	$(1.3 \pm 0.1) \times 10^{-2}$
2009	$(2.3 \pm 0.2) \times 10^{-2}$	–	$(2.3 \pm 0.2) \times 10^{-2}$	–	–	$(2.4 \pm 0.5) \times 10^{-2}$	–	$(2.3 \pm 0.2) \times 10^{-2}$
2009–2011	$(5.9 \pm 0.2) \times 10^{-4}$	$(9.6 \pm 0.8) \times 10^{-4}$	$(5.5 \pm 0.2) \times 10^{-4}$	$(6.8 \pm 1.6) \times 10^{-4}$	–	$(6.2 \pm 0.4) \times 10^{-4}$	$(5.6 \pm 0.5) \times 10^{-4}$	$(5.9 \pm 0.4) \times 10^{-4}$
2013	$(1.3 \pm 0.1) \times 10^{-2}$	–	$(1.3 \pm 0.1) \times 10^{-2}$	–	–	$(1.7 \pm 0.3) \times 10^{-2}$	–	$(1.1 \pm 0.2) \times 10^{-2}$
2014–2015	$(1.9 \pm 0.2) \times 10^{-4}$	$(1.9 \pm 0.2) \times 10^{-3}$	$(1.4 \pm 0.2) \times 10^{-4}$	$(1.3 \pm 0.1) \times 10^{-3}$	–	–	$(1.8 \pm 0.2) \times 10^{-4}$	$(4.0 \pm 0.8) \times 10^{-4}$
Prescription 2: $\mathcal{C}$ derived using ($\dot{M}_{\rm in}$, $R_{\rm in}$) computed by Marcel et al.)								
2002–2003	$(6.6 \pm 0.5) \times 10^{-4}$	$(2.9 \pm 1.2) \times 10^{-3}$	$(5.6 \pm 0.9) \times 10^{-4}$	$(6.4 \pm 1.3) \times 10^{-4}$	$(1.8 \pm 0.4) \times 10^{-3}$	$(1.6 \pm 0.2) \times 10^{-3}$	$(5.2 \pm 0.6) \times 10^{-4}$	$(7.5 \pm 1.0) \times 10^{-4}$
2004–2005	$(1.2 \pm 0.05) \times 10^{-3}$	$(5.0 \pm 0.6) \times 10^{-3}$	$(9.8 \pm 0.6) \times 10^{-4}$	$(1.8 \pm 0.4) \times 10^{-3}$	$(2.8 \pm 0.4) \times 10^{-3}$	$(1.9 \pm 0.2) \times 10^{-3}$	$(1.1 \pm 0.05) \times 10^{-3}$	$(1.4 \pm 0.1) \times 10^{-3}$
2006	$(3.4 \pm 0.2) \times 10^{-3}$	–	$(3.4 \pm 0.2) \times 10^{-3}$	–	–	–	–	$(3.4 \pm 0.2) \times 10^{-3}$
2006–2007	$(4.3 \pm 0.2) \times 10^{-4}$	$(1.8 \pm 0.5) \times 10^{-3}$	$(3.2 \pm 0.3) \times 10^{-4}$	$(6.3 \pm 1.5) \times 10^{-4}$	$(1.2 \pm 0.1) \times 10^{-3}$	$(1.1 \pm 0.2) \times 10^{-3}$	$(3.9 \pm 0.2) \times 10^{-4}$	$(5.9 \pm 0.6) \times 10^{-4}$
2008	$(4.5 \pm 0.4) \times 10^{-3}$	–	$(4.5 \pm 0.4) \times 10^{-3}$	–	–	$(4.4 \pm 0.5) \times 10^{-3}$	–	$(5.2 \pm 0.6) \times 10^{-3}$
2009	$(2.7 \pm 0.1) \times 10^{-3}$	–	$(2.7 \pm 0.1) \times 10^{-3}$	–	–	$(1.4 \pm 0.2) \times 10^{-3}$	–	$(3.9 \pm 0.3) \times 10^{-3}$
2009–2011	$(2.5 \pm 0.1) \times 10^{-4}$	$(5.7 \pm 0.5) \times 10^{-3}$	$(2.5 \pm 0.1) \times 10^{-4}$	$(6.2 \pm 1.1) \times 10^{-4}$	$(1.4 \pm 0.1) \times 10^{-3}$	$(2.8 \pm 0.2) \times 10^{-4}$	$(7.0 \pm 0.6) \times 10^{-4}$	$(1.9 \pm 0.1) \times 10^{-4}$

The time-averaged $\mathcal{C}$ is computed here using an iterative weighted mean technique (see Tetarenko et al. 2016 for details on this statistical method). This technique allows one to take into account the asymmetric (1σ) uncertainties in $\mathcal{C}$.

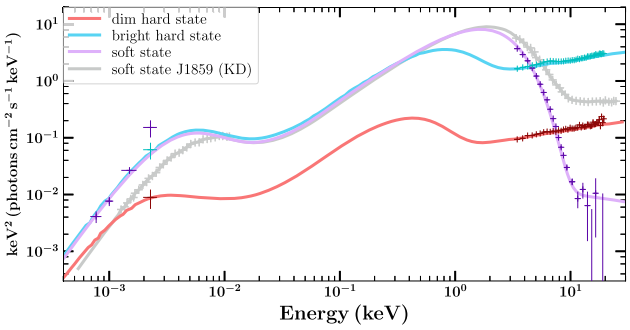

Figure 4. Example SEDs, for selected days near the peak (blue; bright hard-state – MJD 55282), in the soft state plateau (purple; MJD 55464), and during the decay (red; dim hard-state – MJD 55610), of the 2009–2011 outburst. The available SMARTS/ANDICAM data, and 3–40 keV *RXTE*/PCA X-ray spectral data (Clavel et al. 2016), are shown for the soft state observation. To compare our method for computing irradiation properties to the broad-band SED fitting of Kimura & Done 2019 (see discussion in Section 5), we plot: (i) the soft state SED (i.e. data set T3) of XTEJ1859+226, fit with the OPTXRPLIR irradiated disc model of Kimura & Done 2019 (KD; grey), and (ii) the OPTXRPLIR fit to the soft state observation of GX339–4 (purple). The OPTXRPLIR fit to the (jet corrected) *V*-band SMARTS/ANDICAM data, and 3–40 keV *RXTE*/PCA X-ray spectral data, used to compute the irradiation properties with our method, are shown for the two hard-state observations (blue and red).

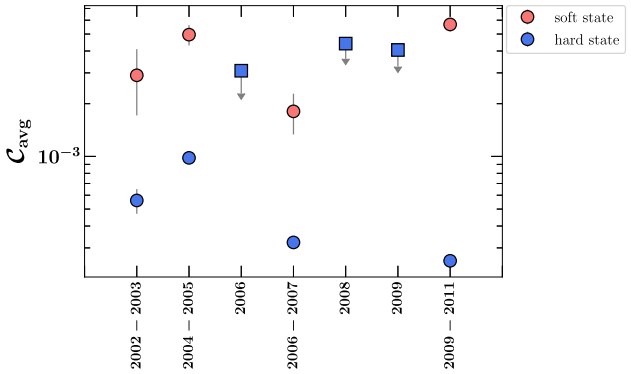

Figure 5. Comparison of the average value of $\mathcal{C}$, computed using the Marcel et al. analysis (see Table 6), during the hard and soft accretion states of our GX339–4 outburst sample. Marker shape specifies outburst classification: canonical (circles) and failed (squares). Hard state $\mathcal{C}$ estimates during failed outbursts are only considered as upper limits, as the optical outburst light curves cannot be corrected for jet contribution (see Section 5 for details).

Unlike the static corona, the wind is expanding. Thus, the rate at which the material in the wind region of the disc ($R > R_{\rm IC}$) is heated, and thus, the condition for which such a wind is launched, will depend both on $L_{\rm X}$ and the irradiating spectrum. The boundary condition between this thermal wind and the corona atmosphere above the disc can be shown to follow (Woods et al. 1996; Done et al. 2018)

$$R_{\rm launch} = \begin{cases} 0.2R_{\rm IC} & L > L_{\rm crit} \\ 0.2\left(\frac{L}{L_{\rm crit}}\right)^{-1} R_{\rm IC} & L < L_{\rm crit}, \end{cases}$$

where

$$L_{\rm crit} \approx 0.09 \left(\frac{10^7\,{\rm K}}{T_{\rm IC}}\right)^{1/2} L_{\rm Edd} \qquad (8)$$

is the critical luminosity which is enough to launch the wind at $R_{\rm IC}$ (i.e. the luminosity that will heat the gas to a temperature $kT_{\rm IC}$ as it reaches a scale height $\sim R$, thus allowing the material to escape).

In principle, the condition for launching such a wind is not only dependent on $L_{\rm X}$ and the irradiating spectral shape, but also on the underlying irradiation geometry (defined via the $\mathcal{C}$ parameter). Begelman et al. (1983) found that this Compton wind, in addition to acting as a mechanism for which mass can be removed from the system, may also act as an effective medium to scatter some of the central X-ray luminosity on to the disc, thus providing a viable irradiation geometry. The irradiation geometry must allow the X-ray flux to irradiate the outer disc. Simple prescriptions, using a radial profile for disc height (e.g. Kim et al. (e.g. Dubus et al. 1999; Kim et al. 1999), show that point source irradiation alone is insufficient to irradiate the outer disc regions. In this situation, the cooler outer region has a smaller scale height than the hotter, inner region, thus is shadowed from the central X-ray source. Therefore, X-ray scattering in a wind above the disc is an attractive solution.

The fraction of intrinsic X-ray flux scattered in this Compton heated wind ($C_{\rm wind}$) can be derived by integrating over the wind column density predicted by Done et al. (2018), yielding (Dubus et al. 2019)

$$C_{\rm wind} = \int_0^1 \int_{R_{\rm in}}^{R_{\rm out}} \eta\sigma_T n_{\rm w}(1-\mu){\rm d}\mu{\rm d}r \approx \frac{\eta\sigma_T \dot{M}_{\rm w}}{8\pi R_{\rm in} v_{\rm w} m_I}, \qquad (9)$$

with η the accretion efficiency (as defined in Section 2.1.1), $n_{\rm w}$ the wind density, $v_{\rm w}$ the mass-weighted wind outflow rate, m_I the mean ion mass per electron, and $\mu = \cos i$, where i is binary inclination (see equation 6 of Done et al. 2018 for details).

We have applied this thermal wind prescription to GX339–4 using: (i) the bolometric luminosity as a function of time, $L_{\rm bol}(t)$, obtained by applying a distance estimate D to the 3–200 keV flux estimated from fitting all available *RXTE*/PCA spectra (see Section 2.1.3), (ii) outer disc radius ($R_{\rm out}$) computed using the defined set of binary orbital parameters (see Appendix A1 and Table 2), and (iii) Compton temperature as a function of time, $T_{\rm IC}(t)$, computed from all available *RXTE*/PCA spectra (see Section 2.1.3), for the outbursts in our sample occurring between 2002 and 2012.

Fig. 6 displays the derived thermal wind properties of: (i) mass-loss rate ($\dot{M}_{\rm wind}$), (ii) launch radii ($R_{\rm launch}$), (iii) velocity ($v_{\rm wind}$), (iv) efficiency ($\eta_{\rm wind}$), (v) column density ($N_{\rm H,\,wind}$), (vi) ionization ($\xi_{\rm wind}$), and (vii) fraction of X-rays scattered in the wind ($C_{\rm wind}$), as a function of time during the 2009–2011 outburst of GX339–4. Note that, for the wind properties shown in this Figure, we assume the system has a random orientation towards us, averaging over all inclination angles. Here, we first compare these wind properties to the time-series evolution of central mass-accretion rate, $\dot{M}_{\rm in}(t)$, derived by Marcel et al.. Then, we compare these wind properties to the reprocessed X-ray fraction ($\mathcal{C}$), derived from the X-ray and optical light curves, using the Marcel et al. derivation of ($\dot{M}_{\rm in}$, $R_{\rm in}$) (see Section 4.1). These results for the remaining 6 outbursts of GX339–4 in our sample considered here, occurring between 2002 and 2012, can be found in Figs D1–D4 in Appendix D.

5.2 The predicted hard and soft state wind in GX339–4

Simple thermal wind models predict that the wind exists in both the hard and soft accretion states during the outbursts of GX339–4 considered here. However, typically BHXBs show that the X-ray spectral signatures of disc winds only exist in the soft state, disappearing as the source transitions into the hard state during

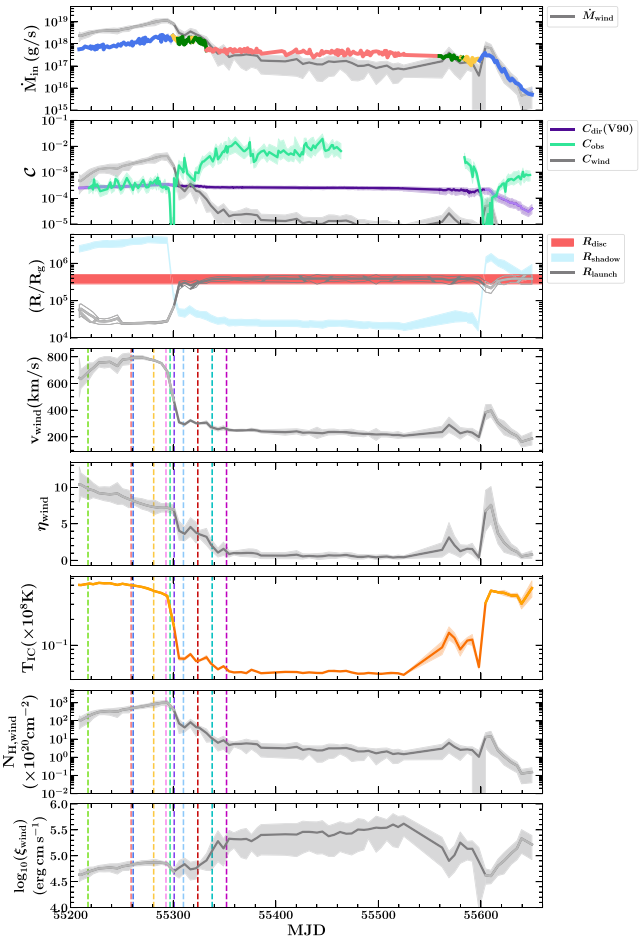

Figure 6. Derived thermally driven (Compton-heated) wind properties for the 2009–2011 outburst of GX339–4. (top) Compares mass-loss rate in the wind ($\dot{M}_{\rm wind}$; grey line), to the central mass-accretion rate ($\dot{M}_{\rm in}$; multicoloured line) on to the BH. The shaded coloured regions here represent the uncertainty in $\dot{M}_{\rm in}$ (see Marcel et al. 2019 for detailed discussion). This panel is colour coded by accretion state as defined by Marcel et al.: red (soft state), yellow (intermediate state; referred to as hard-intermediate state in Marcel et al.), blue (hard state), and green (soft-intermediate state). (second) Compares the fraction of X-rays intercepted and $\mathcal{C}$ as a function of time, computed from the observed X-ray and optical light curves (see Section 3 and Appendix A; green line), via scattering in the wind (see Section 5.1; grey line), and via a direct central source of irradiation [V90; purple line]. See Section 5.3 for details. (third) Displays the launch radii ($R_{\rm launch}$; grey line), and outer disc radii ($R_{\rm disc}$; shaded red region) computed from the chosen set of binary orbital parameters (see Table 2 and Appendix A1), and the radii at which the shadow cast by the inner attenuation zone ends ($R_{\rm shadow}$; see Section 5.1 for discussion), as a function of time. The remaining panels display: (fourth) the wind velocity ($v_{\rm wind}$; in kms^{-1}), (fifth) wind efficiency $\eta_{\rm wind}$ (defined by $\dot{M}_{\rm wind}/\dot{M}_{\rm in}$), (sixth) Compton temperature ($T_{\rm IC}$; in units of 10^8 K) computed by integrating over the best-fitting *RXTE*/PCA spectrum (see Section 2.1.3), (seventh) column density of the wind ($N_{\rm H,\,wind}$; in units of 10^{20} cm^{-2}), and (bottom) log of the ionization of the wind, log$_{10}$($\xi_{\rm wind}$), as functions of time. The shaded coloured regions in all panels represent the 1σ confidence interval propagated for each parameter. The lighter coloured lines/shaded regions in each panel mark times when the outer (irradiated) disc is in the shadow of the inner attenuation zone (i.e. $R_{\rm shadow} > R_{\rm launch}$). The vertical coloured dashed lines in the fourth through bottom panels mark the epochs for which we have simulated X-ray spectra produced by the wind with XSTAR. See Section 5.2.1 for discussion.

outburst (see e.g. Miller et al. 2006b; Ponti et al. 2012; Neilsen 2013; Díaz Trigo et al. 2014). In the case of thermally driven winds, the absence of observed hard state wind signatures relates to the complex response of the wind to the changing illuminating spectral shape. First, the wind is launched from closer in when the spectrum hardens, and secondly, it is irradiated by a much harder spectrum. The combination of these two effects means that the wind is predicted to be completely ionized, so not detectable as absorption lines in X-ray spectra (Chakravorty, Lee & Neilsen 2013; Higginbottom & Proga 2015; Done et al. 2018). This has also been shown in detail in full radiation hydrodynamic simulations as well (Tomaru et al. 2019a, b).

5.2.1 Simulating X-ray spectra produced by the wind during an outburst cycle

We have performed simulations using the XSTAR photoionization code to determine whether spectral features resulting from our predicted hard and soft state thermal wind could be observable in X-ray spectra. We explicitly make use of the XSTAR2XSPEC routine, which creates a table model for use in XSPEC by combining multiple XSTAR simulations for a range of input parameters.

For a multitude of epochs, during state transitions in the four canonical outburst cycles for which detailed spectral information is available, we run the XSTAR2XSPEC routine: (i) using the observed best-fitting spectral model (see details below) as the input continuum SED, (ii) fixing both the density at the wind launch radius[10] (n_0; computed via the thermal wind model) and the (0.0136–13.6 keV) luminosity (L_0; computed from the input continuum SED), (iii) setting the turbulent velocity at 300 kms^{-1} and using solar abundances, and (iv) varying the wind column density ($N_{\rm H,\,wind}$), ionization ($\xi_{\rm wind}$), and line-of-sight velocity ($v_{\rm wind}$).

Fig. 7 shows the resulting simulated X-ray spectra, for 11 individual epochs occurring during the hard–soft state transition of the 2009–2011 outburst of GX339–4. Each simulated spectra here is produced by combining the table model created from the XSTAR2XSPEC routine with: (i) the broad-band (X-ray to UV) spectra from *Swift*/XRT and UVOT (see Reynolds & Miller 2013 for details) to characterize the input continuum SED, and (ii) observable wind properties from the Done et al. (2018) thermal wind model ($N_{\rm H,\,wind}$, $\xi_{\rm wind}$, $v_{\rm wind}$), derived during each particular epoch, assuming three different inclination angles in the range of $37^\circ < i < 78^\circ$ (predicted from optical analysis; Heida et al. 2017). Figs D5–D7 in Appendix D show these results for the hard−soft state transitions occurring during the 2002–2003, 2004–2005, and 2006–2007 outbursts of GX339–4, respectively. In this case, as broad-band *Swift* spectral observations are not available, we characterize the input continuum SED using the available *RXTE*/PCA spectra (see Clavel et al. 2016, for details).

Whether or not it would be possible to observe features from the predicted thermal wind in X-ray spectra is largely dependent on the true binary inclination of GX339–4. While a reliable measurement for binary inclination (e.g. via detection of ellipsoidal modulations) does not yet exist, modelling of the reflection component in X-ray spectra has provided a range of contradictory results. A number

[10]While the Done et al. (2018) wind model assumes gas density varies as $n(R) = n_0(R/R_{\rm launch})^{-2}$, we assume density remains constant with radius. This choice was made because of well-known convergence issues when the above radial dependence for density is used. See https://heasarc.gsfc.nasa.gov/xstar/docs/html/xstarmanual.html for details.

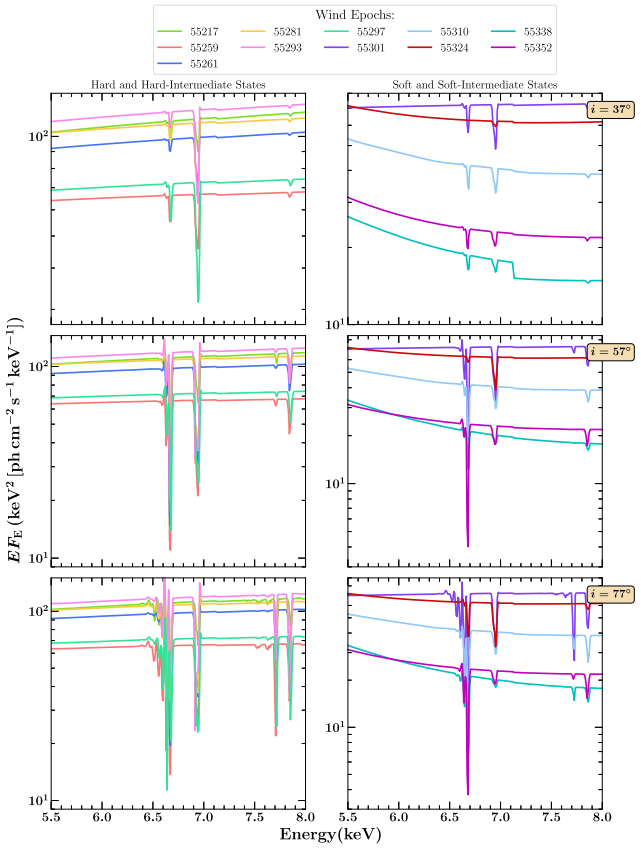

Figure 7. Simulated X-ray spectra of the thermal wind via XSTAR (see Section 5.2.1) for a range of epochs during the 2009–2011 outburst cycle of GX339–4, assuming an inclination of $i = 37°$ (top panels), $i = 57°$ (middle panels), and $i = 77°$ (bottom panels). The wind epochs are split by accretion state for clarity.

of studies making use of a combination of *XMM–Newton* and *RXTE* data, taken during the hard/intermediate states of the 2002–2003, 2004–2005, and 2009–2011 outbursts, uniformly favour a low inclination of $i \sim 10°-20°$ (Miller et al. 2004, 2006b; Reis et al. 2008; Plant et al. 2015). Such a low inclination is consistent with both the independent detection of a one-sided jet (Gallo et al. 2004), and promising evidence for wind spectral features previously detected in emission during the soft state of the 2004–2005 outburst (Miller et al. 2015). On the other hand, by: (i) analyzing the same *XMM–Newton* data (e.g. Done & Diaz Trigo 2010; Basak & Zdziarski 2016), (ii) making use of *Swift* and *NuSTAR* data taken during the 2009–2011, 2013, and 2014–2015 outbursts (Fürst et al. 2015; Parker et al. 2016; Wang-Ji et al. 2018), and (iii) performing an independent analysis of available *RXTE* data in the hard state over a wide range of luminosity (García et al. 2015), other authors derive higher inclination estimates between $i \sim 30°$ and 60°.

It is important to note that reflection modelling is actually measuring the inclination of the inner disc, which does not have to be the same as the binary inclination.[11] Regardless, the predicted absorption features (see Fig. 7 and Figs D5–D7 in Appendix D) are not observed in existing hard or soft state X-ray spectra of GX339–4. The typical equivalent widths (EWs) of these predicted features in our simulated spectra are EW $\gtrsim 15$ eV, for the He-like Fe XXV (6.7 keV) and H-like Fe XXVI (6.97 keV) absorption lines, and thus would be detectable by current missions (e.g. Chandra; see Miller et al. 2006a). Thus, we favour a low inclination of $<37°$. If this is the case, it is unlikely that the predicted (hard- and soft state) thermal wind would ever be observable (at least in absorption) in X-ray spectra of this source.

[11] This situation can happen if, for example, the BH spin angular momentum axis is not aligned with the binary angular momentum vector. Spin-orbit misalignment may be common in BHXBs (see e.g. Atri et al. 2019)

5.3 The role the wind plays during outburst cycles in GX339–4

Taking a time-average over the 2002–2012 period in which our outburst sample covers, we estimate only ~ 25 per cent of the transferred mass escapes in this thermal wind in GX339–4. This low wind mass-loss rate is consistent with the low α-viscosity parameters ($\alpha \sim 0.2$; Tetarenko et al. 2018b) derived from, and expected (from predictions of the DIM) decay time-scales seen in, the observed X-ray light curves of GX339–4.

While this thermal wind, predicted to be present in both the hard and soft accretion states, may not be a dominant mechanism for mass-loss in this system, it does play an important role in the accretion process in terms of irradiating the disc. Using this wind as a medium in which to scatter X-rays back on to the disc, we are able to reproduce some of the features, independently predicted to be present (e.g. Kimura & Done (e.g. Dubus et al. 2019; Kimura & Done 2019), in our computed $\mathcal{C}(t)$ outburst profiles (see Section 4.1). Such features include the peaks/drops in $\mathcal{C}$ occurring during accretion state transitions and complex (day–week time-scale) variability. However, irradiation via scattering in such a thermal wind alone cannot fully account for the $\mathcal{C}$ required to reproduce the observed X-ray and optical light curves throughout entire outburst cycles of GX339–4.

5.3.1 The hard state wind

First, we find whether wind-driven irradiation tends to overpredict the scattering required in the bright hard states of GX339–4. Multiple authors (Begelman et al. 1983; Tomaru et al. 2019a, b) have suggested the possibility that a thermal wind could be intrinsically suppressed in the hard state by the larger shadow cast by the heated inner atmosphere (corona) over the inner disc. Thus, we have investigated the effect that inner corona attenuation would have on our results.

Begelman et al. (1983) were able to show that it is relatively easy for the static corona to become optically thick in the radial direction. Here, an inner attenuation zone forms, with the ability to cast a shadow over the disc surface, strongly affecting the illumination pattern in the outer disc, and in turn the thermal wind properties (Tomaru et al. 2019a, b). The outer disc can only be illuminated when the disc scale height increases enough that it rises above the shadow zone. For an irradiated, isothermal disc [i.e. $H(R) \propto R^{9/7}$, assuming 1/3 of the flux thermalizes in the disc; Cunningham 1976; V90], the radii at which the shadow zone ends can be written as (Tomaru et al. 2019b)

$$R_{\rm shadow} = 3 \times 10^7 \left(\frac{T_{\rm IC}}{10^8 {\rm K}}\right)^{7/8} \left(\frac{M_1}{{\rm M}_\odot}\right)^{1/2} \left(\frac{L}{L_{\rm edd}}\right)^{3/8} \Xi_{\rm h,min}^{-7/8} R_g. \quad (10)$$

In Fig. 6 (as well as the figures in Appendix D), we compare the time evolution of $R_{\rm shadow}$ to the outer disc radius. Given that $R_{\rm shadow}$ is typically $\gtrsim R_{\rm disc}$ during the hard states of GX339–4, there is

considerable uncertainty over the properties of any hard state wind we derive here.

5.3.2 *The soft state wind*

Secondly, we find wind-driven irradiation tends to underpredict the scattering required in the soft states of GX339–4. Thus, we have considered the possibility that a hybrid source of irradiation could exist in this system. Such a configuration would involve irradiation occurring via a combination of (i) scattering in a thermal wind ($\mathcal{C}_{\rm wind}$), and (ii) direct irradiation from a central source of the form (King, Kolb & Szuszkiewicz 1997; Dubus et al. 1999)

$$\mathcal{C}_{\rm dir} = \eta(1-a)\frac{H}{R}\left(\frac{{\rm d}\ln H}{{\rm d}\ln R} - 1\right), \tag{11}$$

where η is accretion efficiency, and a and $H(R)$ are the X-ray albedo and scale height of the disc as a function of radius, respectively. To demonstrate this possibility, in the second panel of Fig. 6 (as well as Figs D1–D4 in Appendix D), we also plot the theoretical estimate of $\mathcal{C}_{\rm dir}$ computed for a isothermal disc (Cunningham 1976), in a LMXB system (V90). However, we caution that this direct irradiation is highly sensitive to the evolution of the disc shape during the outburst. The outer disc is easily shadowed, or the strength of irradiation diminished by the convex shape of the disc, when self consistent calculations are carried out (Meyer & Meyer-Hofmeister 1982; Cannizzo, Chen & Livio 1995; Dubus et al. 1999; Kim et al. 1999).

In doing so, we find that direct irradiation is insufficient to account for the measured $\mathcal{C}$ when the disc enters the soft state and the thermal wind is not dense enough to scatter enough light (Fig. 6). Interestingly, Gandhi et al. (2010) also found a higher than expected reprocessing fraction is required to explain observations of GX339-4. This remains puzzling. One possibility is that our thermal wind model underestimates the wind density in this state. We consider this unlikely given the good agreement generally found between the analytic estimates and more elaborate numerical simulations (see Section 1). Other possibilities include: overestimating the optical contribution from the disc (Section 3.2), leading to a higher effective $\mathcal{C}$ because of contributions from the hotspot, companion or jet (although not in soft state), or a change in albedo or H/R as the disc responds differently to the soft X-ray spectrum.

Given our results, we favour two possible explanations: We are overestimating $\mathcal{C}$ in this source due to seeing it at a low inclination, which also means we underestimate the thermal wind as gravitational redshift reduces the Compton temperature in the observed spectrum compared to that seen by the disc (Muñoz-Darias et al. 2013). Alternatively, there may be an additional source of scattering on to the disc from a magnetic wind. This would need to be completely ionized in order to circumvent the constraints on the wind features discussed above.

6 SUMMARY

While X-ray irradiation of the accretion disc is known to play a key role in regulating the outburst cycles of BHXB systems, how, and to what degree, the discs in these binary systems are irradiated remains largely unknown. The light-curve profiles of BHXB outbursts encode within them distinct observational signatures of the irradiation source heating the disc in the system (King & Ritter 1998; Dubus et al. 2001; Tetarenko et al. 2018a). Accordingly, we have developed a methodology that makes use of a combination of X-ray and optical light curves to track the evolution of physical properties of the X-ray irradiation source heating the discs in these binary systems.

By applying this methodology to ∼15 yr of outburst activity in GX339–4, we are able to derive the evolution of the (i) fraction of the X-ray flux that is intercepted and $\mathcal{C}$, (ii) irradiation temperature at the outer disc radius, $T_{\rm irr}(R_{\rm out})$, over nine individual outburst cycles. In doing so, we find the profiles of $\mathcal{C}(t)$ and $T_{\rm irr}(R_{\rm out}, t)$ throughout individual cycles. These time-series evolutions contain significant variability on time-scales of days to weeks, along with distinct temporal features including, most notably, peaks/drops in $\mathcal{C}$ and $T_{\rm irr}$ that coincide with hard–soft state transitions.

We have first considered a scattering origin for the X-ray irradiation in GX339–4. The (i) observed complex outburst profiles in $\mathcal{C}$ and $T_{\rm irr}$, (ii) typically large derived values of $R_{\rm opt,\,in} \gtrsim 10^5\,R_g$, and (iii) the fact that the distinct temporal features in the BHXB outburst $\mathcal{C}$ profile have previously been associated with irradiation via a thermally driven disc wind (e.g. Dubus et al. 2019), are all suggestive that a disc wind may play a role in irradiating the disc in this system.

Making use of the thermally driven (Compton-heated) wind model of Done et al. (2018), we have: (i) predicted the time-series evolution of key observational properties of this wind, namely, mass-loss rate, launch radii, velocity, column density, ionization, and fraction of X-rays scattered in the wind ($C_{\rm wind}$), and (ii) simulated the X-ray spectra produced by such a wind using the XSTAR photoionization code, for a multitude of epochs during individual state transitions, throughout seven individual outburst cycles.

Contrary to X-ray spectral observations of BHXBs, which typically show disc wind signatures present only in the soft accretion state (Miller et al. 2006b; Ponti et al. 2012; Neilsen 2013; Díaz Trigo et al. 2014), the simple analytic approximation of Done et al. (2018) predicts that the wind exists in both the hard and soft accretion states. We make detailed photoionization models and find that both hard and soft state outflows predict features in the X-ray spectra, in conflict with the observations, unless the source inclination is lower than ∼40°. A low inclination is suggested by both continuum fitting (very low disc temperature; Muñoz-Darias et al. 2013) and X-ray reflection spectroscopy (see e.g. Miller et al. 2004, 2006b; Reis et al. 2008; Plant et al. 2015).

Our findings also suggest this hard and soft state wind is not an efficient mechanism to remove significant amount of mass from the system. In fact, we estimate typically only ∼25 per cent of the transferred mass (from companion star to disc) is lost via such a wind. None the less, the wind may still play an important role as a mechanism for irradiation heating.

Overall, we find that the strength of irradiation ($\mathcal{C}$) required to account for the observed X-ray and optical light curves of GX339–4 is higher than what a combination of thermal wind and direct irradiation can explain. X-ray to infrared global spectral fits of irradiated disc models to individual snapshot observations taking into account all the photometric information can provide a more accurate evaluation of $\mathcal{C}$, and help disentangle the disc and jet contributions, at single points during an outburst. Using this SED fitting method, has allowed us to evaluate additional sources of uncertainty in our method for deriving $\mathcal{C}$. For example, Fig. 4 shows such an SED fit to a soft state observation: Taking into account colour corrections, and allowing for a lower extinction, can reduce the value of $\mathcal{C}$ by a factor 3–4. Even then, neither X-rays scattered in the thermal wind, nor direct X-rays from a central source (when a thermal wind is not dense enough to scatter enough light), can fully explain the magnitude of $\mathcal{C}$ during this soft state.

This is puzzling, as full radiation hydrodynamic simulations of thermal radiative winds have been extremely successful in matching to the observed absorption features in high-inclination, large disc systems such as the BHXB H1743–322 (Tomaru et al. 2019 a, b). It may be that there are substantial differences between the approximate analytic models for thermal winds used here, and the results of full radiation hydrodynamic simulations. Alternatively, it could also be that we underestimate the thermal wind in this source due to seeing it at a low inclination. We will explore these effects in a later work. Tailored radiation hydrodynamic simulations to GX339–4 will enable us to fully assess the scattered flux (via a thermal radiative wind) illuminating the disc in the system. Thus, allowing us to determine whether scattering and direct illumination in a thermal radiative wind can really produce the observed heating of the outer disc, or whether additional mechanisms, such as scattering in a magnetically driven outflow, need to be considered as well.

ACKNOWLEDGEMENTS

The authors would like to thank the anonymous referee for their insightful comments that improved the quality of this manuscript. BET thanks Mark Reynolds for providing his comprehensive broad-band *Swift* spectral results, and Tolga Dincer for providing additional SMARTS data between 2013 and 2015, for GX339–4. BET also thanks Jon Miller for his assistance with, and helpful discussion regarding, the XSTAR simulations and X-ray reflection modelling. BET acknowledges support from the University of Michigan through the McLaughlin Fellowship. GD and MC acknowledge support from the Centre National d'Etudes Spatiales (CNES). This research has made use of: (i) data, software, and/or web tools obtained from the High Energy Astrophysics Science Archive Research Center (HEASARC), a service of the Astrophysics Science Division at NASA Goddard Space Flight Center (GSFC) and of the Smithsonian Astrophysical Observatory's High Energy Astrophysics Division, (ii) data supplied by the UK *Swift* Science Data Centre at the University of Leicester, (iii) data from the SMARTS 1.3 m telescope, (iv) the SVO Filter Profile Service (http://svo2.cab.inta-csic.es/theory/fps/), supported by the Spanish MINECO through grant AyA2014-55216, and (v) NASA's Astrophysics Data System (ADS).

REFERENCES

Atri P. et al., 2019, MNRAS, 489, 3116
Basak R., Zdziarski A. A., 2016, MNRAS, 458, 2199
Begelman M. C., McKee C. F., Shields G. A., 1983, ApJ, 271, 70
Blandford R. D., Königl A., 1979, ApJ, 232, 34
Buxton M. M., Bailyn C. D., Capelo H. L., Chatterjee R., Dinçer T., Kalemci E., Tomsick J. A., 2012, AJ, 143, 130
Cannizzo J. K., 1993, The Limit Cycle Instability in Dwarf Nova Accretion Disks. World Scientific Press, Singapore, p. 6
Cannizzo J. K., Chen W., Livio M., 1995, ApJ, 454, 880
Cannizzo J. K., Wheeler J. C., Ghosh P., 1985, in Lamb D. Q., Patterson J., eds, Astrophysics and Space Science Library Vol. 113, Cataclysmic Variables and Low-Mass X-ray Binaries. Reidel, Dordrecht, p. 307
Cardelli J. A., Clayton G. C., Mathis J. S., 1989, ApJ, 345, 245
Chakravorty S., Lee J. C., Neilsen J., 2013, MNRAS, 436, 560
Chaty S., Dubus G., Raichoor A., 2011, A&A, 529, A3
Chen W., Shrader C. R., Livio M., 1997, ApJ, 491, 312
Clavel M., Rodriguez J., Corbel S., Coriat M., 2016, Astron. Nachr., 337, 435
Corbel S., Fender R. P., 2002, ApJ, 573, L35
Corbel S., Nowak M. A., Fender R. P., Tzioumis A. K., Markoff S., 2003, A&A, 400, 1007
Coriat M., Corbel S., Buxton M. M., Bailyn C. D., Tomsick J. A., Körding E., Kalemci E., 2009, MNRAS, 400, 123
Coriat M., Fender R. P., Dubus G., 2012, MNRAS, 424, 1991
Cunningham C., 1976, ApJ, 208, 534
de Jong J. A., van Paradijs J., Augusteijn T., 1996, A&A, 314, 484
DePoy D. L. et al., 2003, in Iye M., Moorwood A. F. M., eds, Proc. SPIE Conf. Ser. Vol. 4841, Instrument Design and Performance for Optical/Infrared Ground-Based Telescopes. SPIE, Bellingham, p. 827
Done C., Diaz Trigo M., 2010, MNRAS, 407, 2287
Done C., Tomaru R., Takahashi T., 2018, MNRAS, 473, 838
Dubus G., Done C., Tetarenko B. E., Hameury J. M., 2019, A&A, 632, 10,
Dubus G., Hameury J.-M., Lasota J.-P., 2001, A&A, 373, 251
Dubus G., Lasota J.-P., Hameury J.-M., Charles P., 1999, MNRAS, 303, 139
Dubus G., Otulakowska-Hypka M., Lasota J.-P., 2018, A&A, 617, A26
Díaz Trigo M., Migliari S., Miller-Jones J. C. A., Guainazzi M., 2014, A&A, 571, A76
Esin A. A., Kuulkers E., McClintock J. E., Narayan R., 2000b, ApJ, 532, 1069
Esin A. A., Lasota J.-P., Hynes R. I., 2000a, A&A, 354, 987
Evans P. A. et al., 2009, MNRAS, 397, 1177
Falcke H., Biermann P. L., 1995, A&A, 293, 665
Fender R. P., 2001, MNRAS, 322, 31
Ferreira J., Petrucci P. O., Henri G., Saugé L., Pelletier G., 2006, A&A, 447, 813
Foreman-Mackey D., Hogg D. W., Lang D., Goodman J., 2013, PASP, 125, 306
Frank J., King A., Raine D. J., 2002, Accretion Power in Astrophysics, 3rd edn., Cambridge Univ. Press, Cambridge
Froning C. S. et al., 2011, ApJ, 743, 26
Fürst F. et al., 2015, ApJ, 808, 122
Gallo E., Corbel S., Fender R. P., Maccarone T. J., Tzioumis A. K., 2004, MNRAS, 347, L52
Gallo E., Fender R. P., Pooley G. G., 2003, MNRAS, 344, 60
Gandhi P. et al., 2010, MNRAS, 407, 2166
García J. A., Steiner J. F., McClintock J. E., Remillard R. A., Grinberg V., Dauser T., 2015, ApJ, 813, 84
Gierliński M., Done C., Page K., 2009, MNRAS, 392, 1106
Groot P. J., Rutten R. G. M., van Paradijs J., 2001, A&A, 368, 183
Heida M., Jonker P. G., Torres M. A. P., Chiavassa A., 2017, ApJ, 846, 132
Higginbottom N., Proga D., 2015, ApJ, 807, 107
Hogg D. W., Bovy J., Lang D., 2010, preprint (arXiv:1008.4686)
Homan J., Buxton M., Markoff S., Bailyn C. D., Nespoli E., Belloni T., 2005, ApJ, 624, 295
Hynes R. I., 2005, ApJ, 623, 1026
Hynes R. I., Haswell C. A., Chaty S., Shrader C. R., Cui W., 2002, MNRAS, 331, 169
Hynes R. I., Steeghs D., Casares J., Charles P. A., O'Brien K., 2003, ApJ, 583, L95
Hynes R. I., Steeghs D., Casares J., Charles P. A., O'Brien K., 2004, ApJ, 609, 317
Kim S.-W., Wheeler J. C., Mineshige S., 1999, PASJ, 51, 393
Kimura M., Done C., 2019, MNRAS, 482, 626
King A. R., Kolb U., Szuszkiewicz E., 1997, ApJ, 488, 89
King A. R., Ritter H., 1998, MNRAS, 293, L42
Kosenkov I. A., Veledina A., Suleimanov V. F., Poutanen J., 2020, preprint (arXiv:2004.11108)
Lipunova G. V., Malanchev K. L., 2017, MNRAS, 468, 4735
Maccarone T. J., 2014, Space Sci. Rev., 183, 101
Marcel G. et al., 2018a, A&A, 615, A57
Marcel G. et al., 2018b, A&A, 617, A46
Marcel G. et al., 2019, A&A, 626, A115
Markert T. H., Canizares C. R., Clark G. W., Lewin W. H. G., Schnopper H. W., Sprott G. F., 1973, ApJ, 184, L67
McClintock J. E., Horne K., Remillard R. A., 1995, ApJ, 442, 358
McClintock J. E., Remillard R. A., 2006, Black Hole Binaries. Cambridge Univ. Press, Cambridge, p. 157
Meyer F., Meyer-Hofmeister E., 1981, A&A, 104, L10
Meyer F., Meyer-Hofmeister E., 1982, A&A, 106, 34

Migliari S., Fender R. P., 2006, MNRAS, 366, 79
Miller J. M., Fabian A. C., Kaastra J., Kallman T., King A. L., Proga D., Raymond J., Reynolds C. S., 2015, ApJ, 814, 87
Miller J. M., Homan J., Steeghs D., Rupen M., Hunstead R. W., Wijnands R., Charles P. A., Fabian A. C., 2006b, ApJ, 653, 525
Miller J. M. et al., 2004, ApJ, 601, 450
Miller J. M. et al., 2006a, ApJ, 646, 394
Mineshige S., Wheeler J. C., 1989, ApJ, 343, 241
Muñoz-Darias T., Coriat M., Plant D. S., Ponti G., Fender R. P., Dunn R. J. H., 2013, MNRAS, 432, 1330
Neilsen J., 2013, Adv. Space Res., 52, 732
O'Donnell J. E., 1994, ApJ, 422, 158
Osaki Y., 1974, PASJ, 26, 429
Özel F., Psaltis D., Narayan R., McClintock J. E., 2010, ApJ, 725, 1918
Parker M. L. et al., 2016, ApJ, 821, L6
Plant D. S., Fender R. P., Ponti G., Muñoz-Darias T., Coriat M., 2015, A&A, 573, A120
Ponti G., Fender R. P., Begelman M. C., Dunn R. J. H., Neilsen J., Coriat M., 2012, MNRAS, 422, L11
Reis R. C., Fabian A. C., Ross R. R., Miniutti G., Miller J. M., Reynolds C., 2008, MNRAS, 387, 1489
Reynolds M. T., Miller J. M., 2013, ApJ, 769, 16
Russell D. M., Fender R. P., Hynes R. I., Brocksopp C., Homan J., Jonker P. G., Buxton M. M., 2006, MNRAS, 371, 1334
Russell D. M. et al., 2013, MNRAS, 429, 815
Shaw A. W., Tetarenko B. E., Dubus G., Dinçer T., Tomsick J. A., Gandhi P., Plotkin R. M., Russell D. M., 2019, MNRAS, 482, 1840
Shidatsu M., Done C., 2019, ApJ, 885, 14
Smak J., 1983, ApJ, 272, 234
Smak J., 1984, AcA, 34, 161
Subasavage J. P., Bailyn C. D., Smith R. C., Henry T. J., Walter F. M., Buxton M. M., 2010, Silva D. R., Peck A. B., Soifer B.T., eds, SPIE Conf. Ser. Vol. 7737, In Observatory Operations: Strategies, Processes, and Systems III. SPIE, Bellingham, p. 77371C
Suleimanov V. F., Lipunova G. V., Shakura N. I., 2008, A&A, 491, 267
Sunyaev R., Revnivtsev M., 2000, A&A, 358, 617
Tetarenko B. E., Dubus G., Lasota J.-P., Heinke C. O., Sivakoff G. R., 2018a, MNRAS, 480, 2
Tetarenko B. E., Lasota J.-P., Heinke C. O., Dubus G., Sivakoff G. R., 2018b, Nature, 554, 69
Tetarenko B. E., Sivakoff G. R., Heinke C. O., Gladstone J. C., 2016, ApJS, 222, 15
Tomaru R., Done C., Ohsuga K., Nomura M., Takahashi T., 2019b, MNRAS, 490, 3098
Tomaru R., Done C., Ohsuga K., Odaka H., Takahashi T., 2020, MNRAS, 494, 3413
van Paradijs J., 1996, ApJ, 464, L139
van Paradijs J., McClintock J. E., 1994, A&A, 290, 133
Vrtilek S. D., Raymond J. C., Garcia M. R., Verbunt F., Hasinger G., Kurster M., 1990, A&A, 235, 162(V90)
Wang-Ji J. et al., 2018, ApJ, 855, 61
Woods D. T., Klein R. I., Castor J. I., McKee C. F., Bell J. B., 1996, ApJ, 461, 767
Zdziarski A. A., Gierliński M., Mikołajewska J., Wardziński G., Smith D. M., Harmon B. A., Kitamoto S., 2004, MNRAS, 351, 791
Zdziarski A. A., Poutanen J., Mikolajewska J., Gierlinski M., Ebisawa K., Johnson W. N., 1998, MNRAS, 301, 435

SUPPORTING INFORMATION

Supplementary data are available at *MNRAS* online.

Appendix A. The Relationship Between $\dot{M}$ and Absolute Magnitude for Irradiated Accretion discs.
Appendix B. Analysis of OIR Emission Processes During an Outburst Cycle.
Appendix C. Analysis of X-ray Irradiation During Outburst.
Appendix D. Thermally driven Wind Analysis.

Please note: Oxford University Press is not responsible for the content or functionality of any supporting materials supplied by the authors. Any queries (other than missing material) should be directed to the corresponding author for the article.

This paper has been typeset from a TEX/LATEX file prepared by the author.